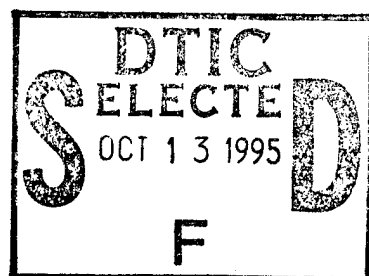# Navier-Stokes Computations of Finned Kinetic Energy Projectile Base Flow

Bernard J. Guidos

ARL-TR-870   September 1995

DTIC
SELECTED
OCT 1 3 1995
F

19951011 146

DTIC QUALITY INSPECTED 5

NOTICES

REPORT DOCUMENTATION PAGE

1. AGENCY USE ONLY *(Leave blank)*	2. REPORT DATE September 1995	3. REPORT TYPE AND DATES COVERED Final, May 1989 - May 1995

4. TITLE AND SUBTITLE

Navier-Stokes Computations of Finned Kinetic Energy Projectile Base Flow

5. FUNDING NUMBERS

1L162618AH80

6. AUTHOR(S)

Bernard J. Guidos

7. PERFORMING ORGANIZATION NAME(S) AND ADDRESS(ES)

US Army Research Laboratory
ATTN: AMSRL-WT-PB
Aberdeen Proving Ground, MD 21005-5066

8. PERFORMING ORGANIZATION REPORT NUMBER

ARL-TR-870

9. SPONSORING/MONITORING AGENCY NAMES(S) AND ADDRESS(ES)

10. SPONSORING/MONITORING AGENCY REPORT NUMBER

11. SUPPLEMENTARY NOTES

12a. DISTRIBUTION/AVAILABILITY STATEMENT

Approved for public release; distribution is unlimited.

12b. DISTRIBUTION CODE

13. ABSTRACT *(Maximum 200 words)*

A computational fluid dynamics (CFD) study of finned kinetic energy projectile base flow is presented for a 105-mm M735 projectile in supersonic flight. A parabolized Navier-Stokes technique is used to compute the attached flow over the forebody and fins. An unsteady Navier-Stokes technique is used to compute the flow in the base region. Several CFD solutions for freestream Mach numbers 3, 4, and 5 are presented, and the modeling approach and computational requirements are discussed. The computed zero-yaw drag coefficients are compared to range-acquired values, and the computed base flow structure is briefly examined.

14. SUBJECT TERMS

computational fluid dynamics, kinetic energy projectile, supersonic flow, aerodynamics

15. NUMBER OF PAGES

56

16. PRICE CODE

17. SECURITY CLASSIFICATION OF REPORT	18. SECURITY CLASSIFICATION OF THIS PAGE	19. SECURITY CLASSIFICATION OF ABSTRACT	20. LIMITATION OF ABSTRACT
UNCLASSIFIED	UNCLASSIFIED	UNCLASSIFIED	SAR

INTENTIONALLY LEFT BLANK.

ACKNOWLEDGMENTS

INTENTIONALLY LEFT BLANK.

TABLE OF CONTENTS

INTENTIONALLY LEFT BLANK.

LIST OF FIGURES

INTENTIONALLY LEFT BLANK.

LIST OF TABLES

INTENTIONALLY LEFT BLANK.

1. INTRODUCTION

The prediction of finned kinetic energy (KE) projectile base flow is a challenging problem in the area of applied computational fluid dynamics (CFD). Finned projectile base flow, even for a non-spinning configuration at 0° angle of attack, is a complex 3-D flow field whose modeling requires the most powerful supercomputing resources available. Accurate modeling of the base flow will provide the base drag coefficient, one of the remaining aerodynamics coefficients yet to be adequately predicted for KE projectiles using CFD. A CFD capability for KE projectile base flow will provide an understanding of the flow structure, possibly leading to the design of effective drag-reduction techniques and lethality enhancements for finned projectiles.

This report documents a CFD study of the base flow of a 105-mm M735 finned KE projectile. Two Navier-Stokes finite difference techniques are used in conjunction to generate flow field solutions at Mach numbers 3, 4, and 5. The major objectives of the study are to (1) numerically simulate the projectile base flow, (2) compare the total computed drag of the projectile with range-acquired data, (3) gain insight into the flow field structure, and (4) characterize the computational requirements of the problem.

An informative overview of projectile CFD work at the U.S. Army Research Laboratory[1] (ARL) is provided by Sturek, Nietubicz, Sahu, and Weinacht (1992). That report traces the development and application of CFD methods for computing KE projectile aerodynamics (excluding the base flow), as well as axisymmetric and 3-D base flows for bodies of revolution. The present study represents the first in-house attempt to model the base flow of a finned projectile using CFD.

2. CONFIGURATIONS AND FLIGHT CONDITIONS

The configuration of interest is the M735 projectile, which is a fin-stabilized, long-rod KE projectile fired from a 105-mm gun tube. The computational model of the M735 projectile, illustrated in Figure 1, is a simplified version of the actual model. The model possesses a conical nose section, followed by a cylindrical section of constant reference diameter, d, equal to 35.2 mm. The total model length is 13.94 calibers (1 caliber = 1 cal = 1 reference diameter). The blunt nosetip is replaced by a conical nosetip, and the sabot grooves are replaced by a smooth surface.

---

[1] Formerly the U.S. Army Ballistic Research Laboratory (BRL)

The six fins are equally distributed around the body and aligned with the projectile axis. The leading edges are cylindrically blunted and swept 71°. The trailing edges are truncated, perpendicular to the projectile axis, and aligned with the projectile base (i.e., no fin overhang). The fins are tapered from root to tip, as shown in Figure 1. The leading and trailing edge chamfers, which control the spin of the actual projectile, are omitted from the computational model. The juncture of the cylinder and the fin leading edge is modified with a small rounded fillet, which typically extends about 0.3 to 0.5 cal upstream and downstream from the juncture. The base of the computational model is assumed to be perfectly flat, in which protuberances such as the tracer cavity and the core rod/finned afterbody interface are ignored.

Computational results are presented for free stream Mach numbers of 3, 4, and 5. The angle of attack is fixed at 0° and the spin rate is fixed at 0 rpm. The free stream conditions are taken to be sea-level atmospheric values. The projectile surface temperature is specified as 294 K or adiabatic, and is discussed in detail later. Fully turbulent boundary layer flow is assumed over the projectile forebody and fins. Laminar flow is assumed in the base region for this initial computational effort.

The roll angle, ϕ, of a point in the flow or on the body is defined as the circumferential angle as measured relative to one reference fin, as illustrated in Figure 2. Since the angle of attack is 0° and the configuration has six fins, only roll angles between 0° and 30° are necessary for clear reference because of circumferential symmetry considerations. For practical purposes, the convention is henceforth adopted that $\phi = 0°$ refers to any of the six circumferential planes ($\phi = 60°$ or $\phi = 180°$, for example) that are coplanar with a fin mid-plane, and $\phi = 30°$ refers to any of the six circumferential planes that are located midway between two adjacent fins. Mirror symmetry in the geometry and flow field is assumed to exist at roll angles $\phi = 0°$ and $\phi = 60°$.

3. FLOW MODEL FOR PROJECTILE FOREBODY AND FINS

The complete flow field surrounding the projectile is computed using two separate 3-D Navier-Stokes numerical techniques in conjunction, as shown in Figure 3. The first is a parabolized Navier-Stokes (PNS) technique, which computes the flow over the projectile forebody and fins. The second is an unsteady Navier-Stokes (UNS) technique, which computes the projectile base flow. The PNS technique is briefly described next; the UNS technique, the application of which is the focus of this research effort, is discussed in some detail thereafter.

2

3.1 Parabolized Navier-Stokes CFD Technique. As shown in Figure 3, the PNS technique is used to provide the upstream inflow boundary condition for the base flow computation. The PNS technique also provides the forebody drag contribution (from the forebody and fins), C_{D_F}, which is added to the base drag contribution (from the cylinder base and fin trailing edge), C_{D_B}, to obtain the total computed zero-yaw drag coefficient, C_{D_O}, that is compared to range-acquired values. The values are tabulated in the results section.

The PNS technique has been adapted and extensively used within the Weapons Technology Directorate of ARL. The original technique was developed by Schiff and Steger (1979), and the first in-house application to U.S. Army projectiles was done by Sturek and Schiff (1981). Applications of the technique to KE and other projectiles have been documented in reports by Rai, Chaussee & Rizk (1983); Weinacht, Guidos, et al (1985, 1986, 1993); Weinacht, et al (1988, 1990, 1991); and Guidos (1994). PNS techniques are space-marching (as opposed to UNS techniques, which are time-marching), in which one numerical integration sweep is made from the nosetip of the projectile to the base to obtain a single steady state solution. Because of this space-marching formulation, PNS techniques are orders of magnitude more computationally efficient than UNS techniques for computing the attached regions of supersonic flow of interest here. The PNS solutions for this configuration were generated using about 1 to 2 hours of central processing unit (CPU) time per solution on a Cray X-MP computer.

This PNS technique is fully implicit, approximately factored (Beam & Warming, 1978), and uses second-order central differencing. In this formulation, only the thin-layer viscous terms in the outward coordinate direction are retained. The Baldwin-Lomax (1978) two-layer algebraic turbulence model is used in all cases presented here. In addition, a shock-fitted outer boundary condition reported by Rai and Chaussee (1983) is used. The code is used in step-back mode to generate a pointed conical nosetip solution, providing the initial conditions for downstream marching, as discussed by Sturek and Schiff (1981).

Typical of long-rod KE projectiles, the actual projectile possesses sabot grooves over the cylindrical forebody section. These grooves act to transfer the accelerating force from the sabot (which also acts as a borerider) to the projectile. The correlation of Mikhail (1989) was used here to estimate the effect of groove drag for the M735 configuration. The correlation shows that the sabot grooves account for, at most, 1.6% of the total drag for Mach numbers between 3 and 5. With this result in hand, all computational drag results presented in this report exclude any contributions from the sabot grooves. As already mentioned, the grooves are replaced by a smooth surface in the computational model.

Two sets of PNS computations were generated. The first set specified the projectile surface temperature to be 294 K. This condition is representative of the temperature of the projectile in early flight, used for obtaining the viscous contribution to the forebody drag. The second set of PNS computations specified the projectile surface temperature condition to be adiabatic, used as the inflow condition for the base flow computations.

4. FLOW MODEL FOR PROJECTILE BASE REGION

4.1 Unsteady Navier-Stokes CFD Technique. The UNS technique is a time-marching scheme, in which an initial assumed flow field is integrated through time toward a steady state solution. The technique used here has previously been described and applied to hypersonic vehicles (Edwards, Chaussee, Lawrence, & Rizk, 1987; Edwards, 1988) and referred to as the UWIN code. The version of the code used here is written in a two-zone grid formulation, as illustrated in Figure 3.

4.2 Governing Equations. The governing equations are a nondimensionalized form of the time-dependent, Reynolds-averaged, thin-layer Navier-Stokes equations in 3-D generalized coordinates and strong conservation law form, given as (Rai 1989)

$$\tilde{Q}_\tau + \tilde{E}_\xi + \tilde{F}_\eta + \tilde{G}_\zeta = R_e^{-1} \tilde{S}_\zeta \tag{1}$$

The generalized curvilinear coordinates are

$\tau = t$ is time

$\xi = \xi(x, y, z, t)$ is the longitudinal (or "streamwise" or "near-axial") coordinate

$\eta = \eta(x, y, z, t)$ is the near-circumferential coordinate

$\zeta = \zeta(x, y, z, t)$ is the outward coordinate

The vector of dependent variables, $\bar{Q}$, is

$$\bar{Q} = J\tilde{Q} = [\rho, \rho u, \rho v, \rho w, \varepsilon]^T \tag{2}$$

in which the density is ρ; the velocity components in the x, y, and z directions are u, v, and w, respectively; and the total energy per unit volume is ε.

4

The vectors $\tilde{E}$, $\tilde{F}$, and $\tilde{G}$ are the transformed inviscid flux vectors:

$$\tilde{E} = J^{-1}\begin{bmatrix} \rho U \\ \rho u U + \xi_x p \\ \rho v U + \xi_y p \\ \rho w U + \xi_z p \\ (\varepsilon + p)U \end{bmatrix} \quad \tilde{F} = J^{-1}\begin{bmatrix} \rho V \\ \rho u V + \eta_x p \\ \rho v V + \eta_y p \\ \rho w V + \eta_z p \\ (\varepsilon + p)V \end{bmatrix} \quad \tilde{G} = J^{-1}\begin{bmatrix} \rho W \\ \rho u W + \zeta_x p \\ \rho v W + \zeta_y p \\ \rho w W + \zeta_z p \\ (\varepsilon + p)W \end{bmatrix} \quad (3)$$

in which U, V, and W are the velocities in the transformed coordinate directions, i.e.,

$$
\begin{aligned}
U &= \xi_x u + \xi_y v + \xi_z w \\
V &= \eta_x u + \eta_y v + \eta_z w \\
W &= \zeta_x u + \zeta_y v + \zeta_z w
\end{aligned}
\quad (4)
$$

Thin-layer viscous terms are retained only in the ζ direction and are contained in the vector $\tilde{S}$, given as

$$\tilde{S} = J^{-1}\begin{bmatrix} 0 \\ m_1 u_\zeta + m_2 \zeta_x \\ m_1 v_\zeta + m_2 \zeta_y \\ m_1 w_\zeta + m_2 \zeta_z \\ m_3 \end{bmatrix} \quad (5)$$

in which

$$
\begin{aligned}
m_1 &= \mu(\zeta_x^2 + \zeta_y^2 + \zeta_z^2) \\
m_2 &= (\mu/3)(\zeta_x u_\zeta + \zeta_y v_\zeta + \zeta_z w_\zeta) \\
m_3 &= (\zeta_x^2 + \zeta_y^2 + \zeta_z^2)[\frac{(a^2)_\zeta}{(\gamma - 1)}(\frac{\mu}{P_r}) + \frac{\mu}{2}(u^2 + v^2 + w^2)_\zeta] \\
&\quad + m_2(\zeta_x u + \zeta_y v + \zeta_z w)
\end{aligned}
$$

$$(6)$$

The following nondimensionalization is used to define the dependent variables:

$$\rho = \frac{\rho^*}{\rho_\infty^*} \qquad u = \frac{u^*}{a_\infty^*/\sqrt{\gamma}} \qquad v = \frac{v^*}{a_\infty^*/\sqrt{\gamma}} \qquad w = \frac{w^*}{a_\infty^*/\sqrt{\gamma}} \qquad \epsilon = \frac{\epsilon^*}{\rho_\infty^* a_\infty^{*2}/\gamma} \qquad (7)$$

in which the superscript " * " denotes a dimensional quantity. Perfect gas behavior is assumed; therefore, the pressure is defined from the dependent variables as:

$$p = (\gamma - 1)[\varepsilon - \frac{1}{2}\rho(u^2 + v^2 + w^2)] \qquad (8)$$

The formulae for the metrics of the coordinate transformation (ξ_t, ξ_x, ξ_y, ξ_z, etc.) and the Jacobian, J, are given by Pulliam and Steger (1978). In regions where turbulence is modeled, the Baldwin-Lomax (1978) model is used.

5

4.3 Numerical Discretization and Solution Algorithm. The governing flow equations are discretized using an approximately factored, implicit, flux-split, upwind, total variation diminishing (TVD), finite difference approach. The scheme, used here to generate steady state solutions, is temporally first order accurate and spatially second order accurate. Applying the scheme to the governing equations yields (omitting most unmodified indices) the following discretization (Rai & Chakravarthy 1986):

$$
\left[I + \frac{\Delta\tau}{\Delta\xi}(\nabla_\xi \tilde{A}^+ + \Delta_\xi \tilde{A}^-)\right]^n \times \left[I + \frac{\Delta\tau}{\Delta\eta}(\nabla_\eta \tilde{B}^+ + \Delta_\eta \tilde{B}^-)\right]^n
$$

$$
\times \left[I + \frac{\Delta\tau}{\Delta\zeta}(\nabla_\zeta \tilde{C}^+ + \Delta_\zeta \tilde{C}^- - R_e^{-1}\delta_\zeta \tilde{N})\right]^n \times (\tilde{Q}^{n+1} - \tilde{Q}^n)
$$

$$
= -\Delta\tau \left[\frac{\hat{E}_{i+1/2}^n - \hat{E}_{i-1/2}^n}{\Delta\xi} + \frac{\hat{F}_{j+1/2}^n - \hat{F}_{j-1/2}^n}{\Delta\eta} + \frac{\hat{G}_{k+1/2}^n - \hat{G}_{k-1/2}^n}{\Delta\zeta}\right]
$$

$$
+ \frac{\Delta\tau}{2\Delta\xi}\left[\Delta E^+(Q_{i-2}, Q_{i-1}, \xi_{i-1/2}) - \Delta E^+(Q_{i-1}, Q_i, \xi_{i+1/2})\right.
$$

$$
\left. + \Delta E^-(Q_i, Q_{i+1}, \xi_{i-1/2}) - \Delta E^-(Q_{i+1}, Q_{i+2}, \xi_{i+1/2})\right]^n
$$

$$
+ \frac{\Delta\tau}{2\Delta\eta}\left[\Delta F^+(Q_{j-2}, Q_{j-1}, \eta_{j-1/2}) - \Delta F^+(Q_{j-1}, Q_j, \eta_{j+1/2})\right.
$$

$$
\left. + \Delta F^-(Q_j, Q_{j+1}, \eta_{j-1/2}) - \Delta F^-(Q_{j+1}, Q_{j+2}, \eta_{j+1/2})\right]^n
$$

$$
+ \frac{\Delta\tau}{2\Delta\zeta}\left[\Delta G^+(Q_{k-2}, Q_{k-1}, \zeta_{k-1/2}) - \Delta G^+(Q_{k-1}, Q_k, \zeta_{k+1/2})\right.
$$

$$
\left. + \Delta G^-(Q_k, Q_{k+1}, \zeta_{k-1/2}) - \Delta G^-(Q_{k+1}, Q_{k+2}, \zeta_{k+1/2})\right]^n + \Delta\tau\left[\frac{\hat{S}_{k+1/2}^n - \hat{S}_{k-1/2}^n}{R_e\Delta\zeta}\right] \quad (9)
$$

in which terms like Δ_ξ, ∇_η, and δ_ζ are forward, backward, and central difference operators, respectively, in the appropriate coordinate direction. The grid point indices i, j, and k correspond to the ξ, η, and ζ directions, respectively. The superscript n represents the current time level, and I is the 5×5 identity matrix.

The implicit (left-hand) side of this equation has been approximately factored (Beam & Warming 1978). The matrices $\tilde{A}^\pm$, $\tilde{B}^\pm$, and $\tilde{C}^\pm$ are the inviscid flux-split Jacobian matrices which relate the changes in the inviscid fluxes with respect to the dependent variables (Pulliam and Steger 1978), evaluated as

$$
\tilde{A}^\pm = \partial(\tilde{E}^\pm)/\partial\tilde{Q} \qquad \tilde{B}^\pm = \partial(\tilde{F}^\pm)/\partial\tilde{Q} \qquad \tilde{C}^\pm = \partial(\tilde{G}^\pm)/\partial\tilde{Q} \quad (10)
$$

The matrix $\tilde{N}$ is the viscous Jacobian matrix corresponding to the ζ direction, whose terms are found using the procedure outlined by Steger (1978).

The explicit (right-hand) side of Eq. (9) includes the vectors $\hat{E}$, $\hat{F}$, and $\hat{G}$, which are first order, inviscid, numerical fluxes; and the vectors $\triangle E^{\pm}$, $\triangle F^{\pm}$, and $\triangle G^{\pm}$, which are flux differences contributing second order spatial accuracy. These vectors, key elements of the numerical scheme, are constructed using the upwind method reported by Chakravarthy and Osher (1983). The flux differences are defined from finite differences evaluated along three subpaths in a state space defined by the Riemann invariants that correspond to the eigenvalues of the Jacobian matrices. The flux differences are then modified using a flux-limiting procedure (Rai and Chakravarthy 1986), and denoted as $\overline{\triangle E^{\pm}}$, $\overline{\triangle F^{\pm}}$, and $\overline{\triangle G^{\pm}}$. Separately, the terms in the viscosity vector $\hat{S}$ are numerically differentiated using standard second-order central differences, as given by Rai (1989).

Equation (9) is a linearized form of the nonlinear governing equations presented in Eq. (1). The nonlinear form of the finite difference equations is solved by applying a Newton-iterative technique (Rai and Chakravarthy 1986). The algorithm can be written as

$$
\left[I + \frac{\Delta\tau}{\Delta\xi}(\nabla_\xi \tilde{A}^+ + \Delta_\xi \tilde{A}^-) \right]^p \times \left[I + \frac{\Delta\tau}{\Delta\eta}(\nabla_\eta \tilde{B}^+ + \Delta_\eta \tilde{B}^-) \right]^p
$$

$$
\times \left[I + \frac{\Delta\tau}{\Delta\zeta}(\nabla_\zeta \tilde{C}^+ + \Delta_\zeta \tilde{C}^- - R_e^{-1}\delta_\zeta \tilde{N}) \right]^p \times (\tilde{Q}^{p+1} - \tilde{Q}^p)
$$

$$
= -\Delta\tau \left[\frac{\tilde{Q}^p - \tilde{Q}^n}{\Delta\tau} + \frac{\hat{E}^p_{i+1/2,j,k} - \hat{E}^p_{i-1/2,j,k}}{\Delta\xi} + \frac{\hat{F}^p_{i,j+1/2,k} - \hat{E}^p_{i,j-1/2,k}}{\Delta\eta} + \frac{\hat{G}^p_{i,j,k+1/2} - \hat{G}^p_{i,j,k-1/2}}{\Delta\zeta} \right]
$$

$$
+ \frac{\Delta\tau}{2\Delta\xi} \left[\overline{\triangle E^+}(Q_{i-2}, Q_{i-1}, \xi_{i-1/2}) - \overline{\triangle E^+}(Q_{i-1}, Q_i, \xi_{i+1/2}) \right.
$$

$$
\left. + \overline{\triangle E^-}(Q_i, Q_{i+1}, \xi_{i-1/2}) - \overline{\triangle E^-}(Q_{i+1}, Q_{i+2}, \xi_{i+1/2}) \right]^p
$$

$$
+ \frac{\Delta\tau}{2\Delta\eta} \left[\overline{\triangle F^+}(Q_{j-2}, Q_{j-1}, \eta_{j-1/2}) - \overline{\triangle F^+}(Q_{j-1}, Q_j, \eta_{j+1/2}) \right.
$$

$$
\left. + \overline{\triangle F^-}(Q_j, Q_{j+1}, \eta_{j-1/2}) - \overline{\triangle F^-}(Q_{j+1}, Q_{j+2}, \eta_{j+1/2}) \right]^p
$$

$$
+ \frac{\Delta\tau}{2\Delta\zeta} \left[\overline{\triangle G^+}(Q_{k-2}, Q_{k-1}, \zeta_{k-1/2}) - \overline{\triangle G^+}(Q_{k-1}, Q_k, \zeta_{k+1/2}) \right.
$$

$$
\left. + \overline{\triangle G^-}(Q_k, Q_{k+1}, \zeta_{k-1/2}) - \overline{\triangle G^-}(Q_{k+1}, Q_{k+2}, \zeta_{k+1/2}) \right]^p + \Delta\tau \left[\frac{\hat{S}^p_{k+1/2} - \hat{S}^p_{k-1/2}}{R_e \Delta\zeta} \right] \quad (11)
$$

In Eq. (11), $\tilde{Q}^p$ is an approximation to $\tilde{Q}^{n+1}$. Whereas the superscript n represents the current time level, the superscript p represents the iteration number for the current time level. When $p=0$, then $\tilde{Q}^p = \tilde{Q}^n$, and when Eq. (11) is iterated to convergence at a given time step, then $\tilde{Q}^p = \tilde{Q}^{n+1}$. In the present study, in which steady state solutions were

sought, two iterations per time step were executed in all cases. As discussed by Rai and Chakravarthy (1986), one primary advantage of the iterative approach is that the stability of the system of equations is enhanced, allowing larger time steps to be taken than with non-iterative approaches. One disadvantage of the iterative approach is the increased computer memory requirement of needing to store both $\tilde{Q}^n$ and $\tilde{Q}^p$.

4.4   Boundary and Initial Conditions

Non-Zonal Boundaries

As already mentioned, the inflow boundary conditions for Zone 1 are generated by a PNS computation which provides the flow conditions at an axial position upstream from the projectile base. The outer boundary points of Zones 1 and 2 are assigned free-stream values and located beyond the bow shock, which is captured within the interior of the computational domain. The downstream outflow boundary (Zone 2) is specified using a first order extrapolation of the dependent flow variables. Circumferential boundary conditions are applied in both zones by employing symmetry principles on the two planes corresponding to roll angles $\phi = 0°$ and $\phi = 30°$.

Adiabatic boundary conditions are applied along all solid surface boundaries. The no-slip boundary condition is enforced, and a zero normal pressure derivative is imposed. First order implicit boundary conditions are implemented (Rai 1989).

Zone 2 inner boundary points are assigned values that depend upon whether a miniature sting or an axis boundary is prescribed within the flow domain. The miniature sting is treated as a solid, adiabatic surface. The axis boundary is handled using the following first order boundary conditions which are applicable to zero-yaw flight conditions:

$$\rho_1 = \rho_2 \qquad u_1 = u_2 \qquad v_1 = 0 \qquad w_1 = 0 \qquad p_1 = p_2 \tag{12}$$

in which the subscripts 1 and 2 refer to the axis boundary point and first interior grid point, respectively, along a radial grid line. For the three-dimensional flow situation in this study, the above relationships yield multi-valued axis grid points. The mean values of each of these variables are calculated and used at all coincident axis points; the fifth dependent variable, ϵ, is then determined from the perfect gas relationship.

Zonal Boundaries

In the present grid configuration, the zonal boundary interface, consisting of two overlapping boundaries, is located at the projectile base. Specifically, the two zonal boundaries

correspond to the Zone 1 outflow plane and the Zone 2 inflow plane. Both zonal boundaries are perpendicular to the projectile axis and overlap each other by one or more grid points, as shown in Figures 3 and 4. The Zone 2 zonal boundary is coplanar with the base, the fin trailing edge, and the next-to-last downstream grid plane of Zone 1. The Zone 1 zonal boundary is located downstream from the base and fin trailing edge and is constructed to be coplanar with either the first or one of the first upstream interior grid planes of Zone 2. Since the zonal boundary points do not match those of the overlapping grid, it is necessary to interpolate the values of the dependent variables within each zonal boundary plane.

In the present study, an explicit, triangular, Cartesian interpolation procedure is used. The procedure is nonconservative and depends solely on the grid geometries, and so the interpolation coefficients associated with each zonal boundary point are only calculated at the onset of the computation. The procedure is illustrated in Figure 5, in which P is a zonal boundary point whose dependent variables are to be defined using points 1, 2, and 3 from the neighboring zone. Point P is assumed to be coplanar with and encompassed by points 1, 2, and 3. In the current approach, one of the three points is point P's closest neighbor. Point O is defined by points 1, 2, and 3 so that it forms the origin of a right-handed, orthogonal, sub-coordinate system defined by unit vectors $\hat{e}_1$, $\hat{e}_2$, and $\hat{e}_3$. Let f represent a scalar quantity (ρ or ϵ, for example); then its value at point P is denoted f_P and is found from

$$f_P = C_1 f_1 + C_2 f_2 + C_3 f_3 \tag{13}$$

In this equation, f_1, f_2, and f_3 are the current, known values of f at points 1, 2, and 3, respectively; and C_1, C_2, and C_3 are interpolation coefficients given by

$$C_n = \bar{r}_P \cdot \hat{e}_n \qquad \text{for} \qquad n = 1, 2, \text{ and } 3 \tag{14}$$

in which the vector $\bar{r}_P$ represents the vector extending from point O to point P.

The interpolation procedure is not applied to those Zone 2 boundary grid points which are surface points, i.e., that constitute the projectile base or fin trailing edge. Those points are instead flagged at the onset of the computation and are updated using the adiabatic, no-slip boundary procedure already mentioned.

Initial Conditions

Initial conditions had to be generated anew at least once at each Mach number. For a time-iterative problem of this magnitude, the initial conditions can significantly impact the computer time needed for the solution to approach a steady state. Zone 1 initial conditions were straightforward because of the availability the PNS solutions. Zone 2 initial conditions proved to be more sensitive, since free stream or outer flow initial values caused major numerical instabilities to arise in almost all cases when they were used.

An alternate initialization procedure was implemented as follows: The Zone 1 dependent variables at all axial locations are assigned values from the inflow plane using

$$f_{i,j,k} = f_{1,j,k} \tag{15}$$

The Zone 2 inflow dependent variables are obtained by applying the zonal boundary interpolation scheme at all zonal boundary points, as previously described. The cylinder base and fin trailing edge surface grid points are assigned zero velocity, free stream total energy, and density values from the perfect gas relation. Next, the Zone 2 outflow variables are assigned free stream values. Finally, the interior grid points are assigned values by interpolating between the Zone 2 inflow and outflow grid planes.

5. COMPUTATIONAL DATA SETS AND GRIDS

5.1 Overview

Results from six CFD solutions are discussed herein and are introduced in Table 1. All but one of the data sets were generated on a Cray X-MP/48 computer (formerly located at Aberdeen Proving Ground [APG]), using one processor and limited to 2 million words (2 Mw) of memory. Upon transfer from NASA Ames Research Center, Moffett Field, California, the UWIN code was configured to load into core memory and process one and only one zone at a time to increase the number of allowable grid points in each of the two zones. The most recent, and final, solution data set of the study (Solution 3-B) was generated on a Cray-2 computer located at APG, using approximately 11 Mw of the 256 Mw of available memory. The data sets generated on the Cray X-MP used about 200 CPU hours each, and the data set generated on the Cray-2 used about 1200 CPU hours.

Tables 2 and 3 list the values of the important grid parameters that were used for each solution, and these parameters are illustrated in Figure 4. Examples of actual grids are shown in Figures 6, 7, and 8. Grid clustering is evident in several areas and in all three coordinate directions. In any given direction, the magnitude of the grid point clustering factor, F_l, was kept within ± 20% (but usually within ± 15%) for all solutions presented here. The clustering factor is defined here as

$$F_l = \frac{\Delta s_{l+1} - \Delta s_l}{\Delta s_l} \times 100\% \tag{16}$$

in which Δs_l and Δs_{l+1} are adjacent grid point spacings between grid indices l and $l + 1$ in any of the three computational coordinate directions.

Table 1. Base Flow Computational Solution Data Sets

Data Set	M_∞	Computer	Data Set Size (Mb)	Job Size (Mb)	CPU Seconds per Time Step
3-A	3.0	Cray X-MP	10.5	1.8	21.
3-B	3.0	Cray 2	66.0	11.3	147.
4-A	4.0	Cray X-MP	3.6	0.6	6.
4-B	4.0	Cray X-MP	10.5	1.8	18.
4-C	4.0	Cray X-MP	10.5	1.8	21.
5-A	5.0	Cray X-MP	10.5	1.8	21.

Table 2. Grid Parameters - Zone 1

(All distances and lengths in calibers)

Data Set	Grid Points axial×circ×out	x_{in}	Δx_{fin}	Δs_{wall} $\times 10^5$
3-A	$10 \times 35 \times 45$	13.36	.064	5.8
3-B	$30 \times 35 \times 45$	13.36	.00036	5.8
4-A	$8 \times 25 \times 45$	13.36	.082	72.0
4-B	$10 \times 35 \times 45$	13.36	.064	5.8
4-C	$10 \times 35 \times 45$	13.36	.064	5.8
5-A	$10 \times 35 \times 45$	13.36	.064	4.3

Table 3. Grid Parameters - Zone 2

(All distances and lengths in calibers)

Solution Name	Grid axial×circ×out	x_{out}	Δx_{base}	Sting Radius	Δr_0	Δr_1	Δr_2	No. T.E. Points
3-A	$30 \times 35 \times 75$	17.91	.0144	none	.0043	.0043	.022	10
3-B	$54 \times 71 \times 160$	17.91	.00036	none	.0043	.0043	.072	15
4-A	$24 \times 25 \times 45$	18.77	.082	.00072	.0036	none	none	2 to 4
4-B	$25 \times 35 \times 90$	16.10	.0144	.00072	.0036	.0022	.022	10
4-C	$30 \times 35 \times 75$	17.91	.0144	none	.022	.0022	.022	10
5-A	$30 \times 35 \times 75$	17.91	.0144	none	.0043	.0043	.022	10

11

Figure 6 shows a $\phi = 0°$ grid slice of the PNS grid (in which only a few of the axial stations in the region are shown), as well as the Zone 1 and Zone 2 grids of Solution 4-C. Without exception, the gridding is comprised of 2-D computational grid planes aligned perpendicular to the projectile axis. In Zone 1, axial grid point spacing is constant except for Solution 3-B, where points were clustered near the base. In Zone 2, axial grid point clustering is prescribed near the projectile base and radial grid point clustering is prescribed at three radial locations: (1) the axis (or miniature sting), (2) the cylinder edge, and (3) the fin tip.

Figure 7 shows a cross section of the Zone 1 grid of Solution 3-B. Each Zone 1 grid cross section is a planar elliptic grid constructed using the same approach as the PNS grid. Grid points are equally distributed in the axial direction, with the exception of Solution 3-B, which clusters the points axially near the base. Grid points are also radially clustered near the forebody and fin surfaces to adequately resolve the attached boundary layer. The distance from the wall to the first interior grid point in Zone 1 was determined from the PNS solutions, which used the adaptive grid procedure discussed by Sturek and Schiff (1981). The value of the boundary layer coordinate, y^+, at the first point from the surface is maintained in the range from 2 to 5.

Figure 8 shows a cross section of the Zone 2 grid of Solution 3-B. Each Zone 2 grid cross section is algebraically constructed. The Zone 2 grid is designed so that one grid line on the inflow boundary extends piecewise continuously from the axis to the outer boundary and is coincident with the fin planform edge, at least along the straight section. Such construction aligns the grid with most of the fin planform edge, allowing the fin boundary layer to be better resolved as it separates from the trailing edge and forms a free shear layer. Grid points are circumferentially clustered between this fin edge and $\phi = 30°$. Grid points are equally distributed across the thickness of the trailing edge, with the exception of Solution 3-B, which clusters the trailing edge points near the fin planform edge.

5.2   Details of Data Sets

The discussion of the individual CFD data sets begins at Mach 4, the free stream velocity of the initial problem setup upon transfer from NASA Ames. The data sets are described here in mostly chronological order by first discussing the Mach 4 cases, followed by the Mach 3 cases, then the Mach 5 case.

Solution 4-A, at Mach 4, is the first solution generated in the study that includes the projectile base region. It is chronologically the first solution to be generated of the six solutions presented here. The grid resolution for Solution 4-A, as apparent from Table 3, is considerably less than the other five CFD solutions. The Zone 2 outward grid lines of Solution 4-A are oriented along constant ϕ values, as opposed to being aligned with the fin planform edge. Solution 4-A also includes a miniature sting, since the axis boundary condition had yet to be implemented. Solution 4-A was successfully initialized using free-stream values for the interior grid points.

Solution 4-B, also at Mach 4, is the first of the study to radially cluster points at three radial locations: the axis, the projectile cylinder edge, and the fin tip. It is also the first solution to circumferentially align the Zone 2 grid with the fin planform edge, as was illustrated in Figure 6. Like Solution 4-A, it includes a miniature sting. The outflow boundary of Solution 4-B was moved upstream by 2.67 cal compared to that of Solution 4-A in an effort to save grid points. Solution 4-B was initialized using the alternate procedure described earlier.

Solution 4-C, the third and final solution at Mach 4, is the first solution of the study to include the axis boundary condition. The Zone 2 radial grid spacing and distribution were modified slightly compared to Solution 4-B. Also, the outflow boundary was moved downstream by 1.81 cal compared to that of Solution 4-B since it was noticed that Solution 4-B had regions of subsonic velocity in the outflow plane. Solution 4-C was initialized by interpolating the dependent variables from Solution 4-B.

Solution 3-A, at Mach 3, includes all the features of Solution 4-C, with the exception of minor differences in Zone 2 grid spacing and distribution (see Table 3). Solution 3-A was initialized using the alternate procedure described earlier.

Solution 3-B, also at Mach 3, is chronologically the last solution to be generated during the study. It has almost six times more grid points in Zone 2 (over 600,000 total) than the other data sets. The additional grid points were used to increase the near wall resolution in the axial and circumferential directions. The number of grid points across the trailing edge half-thickness was 15, and Solution 3-B was the only data set to circumferentially cluster these trailing edge points along the fin planform edge. Solution 3-B was initialized by interpolating the dependent variables from Solution 3-A.

Solution 5-A, the only solution at Mach 5, has the same modeling and grid features as Solutions 3-A and 4-C. Solution 5-A was initialized using the alternate procedure described earlier.

6. RESULTS

6.1 Drag Comparison. The range-acquired drag coefficients (see Table 4) were obtained from unpublished firings conducted at the indoor ARL transonic range facility at APG during 1979. The 14 shots listed here were fired with an empty tracer cavity. The zero-yaw drag coefficients were produced from standard yaw-drag fits of the equations of motion from Murphy (1963). The total drag coefficient, C_D, of a projectile at some instant in time is defined as

$$C_D = C_{D_O} + C_{D_{\delta^2}}\delta^2 \tag{17}$$

in which C_{D_O} is the zero-yaw drag coefficient, $C_{D_{\delta^2}}$ is the yaw drag coefficient, and δ is the angle of attack. The set of 14 fitted values of C_D and δ were used to make a least squares fit to the equation

$$C_D = A_1 + \frac{A_2}{M_\infty} + C_{D_{\delta^2}}\delta^2 \tag{18}$$

in which values of A_1 and A_2 (coefficients of no interest here), as well as $C_{D_{\delta^2}}$, were obtained. The Mach number for each shot is M_∞. The resulting value of 14.6 for $C_{D_{\delta^2}}$ was then used to repeat the yaw-drag fits to obtain C_{D_O}.

Table 4. Range-Acquired Zero-Yaw Drag Coefficients

Shot No.	M_∞	C_{D_O}	Shot No.	M_∞	C_{D_O}
16405	4.295	0.295	16417	4.113	0.305
16423	4.289	0.293	16401	3.873	0.324
16404	4.281	0.302	16402	3.869	0.327
16424	4.262	0.300	16403	3.759	0.342
16421	4.237	0.303	16419	3.447	0.372
16422	4.223	0.305	16418	3.437	0.368
16416	4.123	0.306	16420	3.015	0.420

Table 5 lists the computed zero-yaw drag coefficients and various components for the six CFD data sets. As mentioned earlier, the computed zero-yaw drag coefficient, C_{D_O}, is defined as

$$C_{D_O} = C_{D_F} + C_{D_B} \tag{19}$$

in which C_{D_F} is the forebody drag contribution (which includes the forebody and fin contribution, i.e., the attached flow) obtained from the PNS code, and C_{D_B} is the base drag contribution (which includes the cylinder base and fin trailing edge drag contribution) obtained from the UNS code. The computed drag coefficients are calculated by using the force

14

Table 5. Computed Zero-Yaw Drag Coefficients

M_∞	C_{D_F} (PNS)	Data Set (UNS)	C_{D_B} (UNS)	C_{D_O}	$(p_B/p_\infty)_{avg}$
3.0	0.240	3-A	0.123	0.363	0.463
"	"	3-B	0.143	0.383	0.376
4.0	0.222	4-A	0.047	0.269	0.636
"	"	4-B	0.084	0.306	0.349
"	"	4-C	0.082	0.304	0.364
5.0	0.202	5-A	0.047	0.249	0.433

acting on the entire base and six fins of the projectile, consistent with the range-acquired drag coefficients. At Mach 4, the computed base drag of Solution 4-A (the coarsest grid of the six CFD data sets) is about 56% of that of Solutions 4-B or 4-C. The computed base drag of Solutions 4-B and 4-C themselves differs by less than 3%. At Mach 3, the base drag of Solution 3-B (the finest grid of the six CFD data sets) is about 15% greater than that of Solution 3-A.

Figure 9 shows the comparison of computed and range-acquired zero-yaw drag coefficients. The results of Solutions 3-B, 4-C, and 5-A are combined with the PNS results (also shown) in the figure. The computed drag underpredicts the range-acquired drag by about 9% and 5%, at Mach 3 and 4, respectively. Since no firings were conducted above Mach 4.3, no comparison can be made for the Mach 5 case. The computed base drag comprises about 33%, 26%, and 19% of the computed total drag at Mach 3, 4, and 5, respectively.

Though the drag comparison serves as an initial indicator of the accuracy of the CFD approach, more precise validation of the predicted flow field is needed. The focus of future research in this area should be the validation of base and fin trailing edge pressure predictions against wind tunnel measurements such as those reported by Berner et al. (1992) or cited by Moore et al. (1993). While no further quantitative comparisons are made in this report, some details of the computed base flow structure are presented.

6.2 Base Pressure. Table 5 also includes the average base pressure, $(p_B/p_\infty)_{avg}$, for each of the six CFD solutions. The average base pressure consists of the cylinder base and fin trailing edge contributions. A comparison of Solutions 3-A, 4-B, and 5-A, which basically have the same grid resolution, reveals that the computed average base pressure of Mach 5 is less than that of Mach 3 but greater than that of Mach 4. Such non-monotonic behavior

with respect to free stream Mach number is unexpected, at least for axisymmetric base flows as well as 2-D trailing edge flows. The result does not specifically eliminate the possibility that interaction between the axisymmetric-like cylinder base and 2-D-like trailing edge could produce such behavior but should be viewed as a possible inconsistency between solutions. The result may be attributable to inadequate grid resolution, modeling assumptions, or insufficient convergence of one or more of the CFD solutions. A conclusive interpretation cannot be made without quantitative pressure measurements with which to compare.

Figures 10 through 14 show the computed base pressure distributions along roll angles $\phi = 0°$ and $\phi = 30°$ for each of the six CFD solutions. At Mach 4, Solution 4-A has much higher base pressures than Solutions 4-B and 4-C, almost certainly attributable to its comparatively sparse grid. Solution 4-B has a lower base pressure on the cylinder portion than Solution 4-C, but the trend is reversed on the fin trailing edge, and the integrated effect leads to the similar base drag values for the two solutions, as already shown. At Mach 3, this same pressure reversal on cylinder base and fin trailing edge is found between Solutions 3-A and 3-B.

All the CFD solutions except Solution 5-A show higher pressure along the fin trailing edge than on the cylinder base. Along $\phi = 30°$, all six CFD solutions show at least a slight undershoot in pressure near the cylinder edge, indicative of a possible need for improved grid resolution there. The same observation may apply along $\phi = 0°$ near the fin tip. For each CFD solution, small differences between pressure distributions along $\phi = 0°$ and $\phi = 30°$ are apparent, but the details are inconsistent; in some cases, higher pressures exist along $\phi = 0°$ than $\phi = 30°$, and in other cases, the opposite is true. Of all the pressure distributions shown here, that of Solution 3-B has the most apparent saddle points, probably attributable to its finer grid resolution compared to the other five CFD solutions.

6.3 Flow Structure

Mach 4 / Mach 4.3

Figure 15 is a reproduced shadowgraph mosaic of an M735 projectile at Mach 4.3, taken at the ARL transonic range facility during a nosetip boundary layer transition study reported by Sturek, Kayser, and Mylin (1983). The shadowgraph, discovered late in the present study, is included here to at least qualitatively compare with Solution 4-C, which is at Mach 4.0. The film surface is estimated to be parallel to roll angle $\phi = 24°$ within $\pm 3°$.

Two main features apparent in the base region of the shadowgraph are (1) a turbulent flow region extending practically from tip-to-tip of opposite fins and (2) two or three shocks

emanating from an axial location near the cylinder base above and below the projectile axis. The shocks are oriented at approximately 10° relative to the axis. The two shocks nearest to the axis almost appear to intersect the axis at about 1 cal down stream from the base. From the shadowgraph alone, an observer cannot conclusively determine whether all the shock images in the cylinder base region represent structures that are coplanar with the $\phi = 24° \pm 3°$ plane, as opposed to being parallel to it.

Figures 16 and 17 show computed Mach contours for Solution 4-C in the $\phi = 0°$ and $\phi = 30°$ planes. In the $\phi = 0°$ plane, a well defined velocity wake region is apparent from tip-to-tip of opposite fins. The velocity wake region is also well-defined in the $\phi = 30°$ plane, contracting to a minimum width of about 3/4 cal at about 3/4 cal downstream, and expanding to a maximum width of about 1.5 cal at about 3 cal downstream. Both roll angles show a small core (widths on the order of 1/10 cal) of low Mach number flow extending downstream along the axis. Both roll angles also show the width of this core to noticeably increase about 3 cal downstream from the base, especially in the $\phi = 0°$ plane.

Figures 18 and 19 show computed pressure contours for Solution 4-C in the $\phi = 0°$ and $\phi = 30°$ planes. Some qualitative similarity in the location and orientation of shocks can be discerned between Solution 4-C and the shadowgraph. In the CFD solution, the shock structures more closely resemble recompressions since they are highly smeared (and somewhat step-like in shape), probably attributable to inadequate grid resolution. As in the shadowgraph, the computed shock structures are oriented at approximately 10° relative to the axis. They are more pronounced in the $\phi = 30°$ plane than in the $\phi = 0°$ plane, and those nearest the axis extend no farther upstream than about 1 cal from the base. In addition, the pressure contours in both planes show a region of relatively compressed flow along the axis beginning 0.5 cal downstream of the base and extending about 1.5 cal farther downstream.

In the previous figures, no major discontinuities are apparent in the contour lines that intersect the zonal boundary interface. On a smaller scale, however, it is noted that some minor numerical disturbances were introduced into all from the flow solutions near the curved edges of the base and fin trailing edge. Two likely causes of these disturbances are (1) the use of the current zonal boundary interpolation scheme in conjunction with such relatively sparse grid resolution in the vicinity of the solid boundaries, and (2) the use of fully turbulent flow conditions in Zone 1 and fully laminar flow conditions in Zone 2 introducing an additional flow discontinuity to numerically capture.

Mach 3

Of the six CFD solutions discussed in this report, Solution 3-B, at Mach 3, has the most grid points and best spatial resolution. Figures 20 through 22 show Mach contours, pressure contours, and velocity vectors, respectively, in the $\phi = 0°$ and $\phi = 30°$ half-planes of Zone 2. In these figures, the two half-planes are presented perpendicular to each other, with the $\phi = 0°$ half-plane above the axis. These figures show a closer view of the flow near the base than the Mach 4 case just shown.

In the $\phi = 0°$ half-plane, Figures 20 and 21 show one shock structure emanating from a location near the axis at an angle of approximately 30° relative to the axis. This is in contrast to the Mach 4 case just shown, which had two shock structures in each half-plane. As in the Mach 4 case, smearing and step-like behavior is apparent in the Mach and pressure contours that comprise this computed shock structure. The shock structure practically intersects the axis at a location about 1 cal downstream from the base. There, a compressed low Mach number region of axial length about 1/2 cal and extending 1/10 cal in the radial direction is apparent in both half-planes. Downstream, the contours intersect the axis in a more perpendicular fashion than do those of the Mach 4 solution already shown.

In Figure 22, the flow directly downstream from the fin trailing edge moves strongly toward the axis and meets outwardly moving flow from the cylinder base region. Figures 20 and 22 show that the flow from these two regions is separated by a weak shear layer oriented about 30° relative to the axis.

In the $\phi = 0°$ half-plane, Figure 22 shows a small region of reverse flow (that is, in which the axial velocity component is oriented upstream) within 1/2 cal downstream from the fin. Within the cylinder base region itself, no reverse flow is computed to occur within 1/2 cal from the base, indicating that the fluid is entering the $\phi = 0°$ half-plane near the base. Approximately 1 cal farther downstream in the $\phi = 0°$ half-plane, reverse flow is apparent, indicating that the fluid is exiting the $\phi = 0°$ half-plane.

In the $\phi = 30°$ half-plane, Figure 22 shows reverse flow within 1/4 cal from the base. The reverse flow is part of a recirculation zone whose center marks the upstream edge of a shear layer. The shear layer, located approximately 1/4 cal from the axis, separates the reversed and non-reversed flow regions and extends farther downstream. The free shear layer that enters the $\phi = 30°$ plane from the cylinder surface is shown to largely dissipate by the time the flow reaches 1 cal downstream.

Figure 23 shows computed axial velocity contours for Solution 3-B at six cross-sectional planes downstream from the base. The axial velocity, u, is normalized by the free stream

speed of sound, a_∞. The farthest downstream plane is located approximately 1 cal from the base. For purposes of orientation, the projectile axis is plotted as a thick solid line. In the figure, black contour lines represent negative axial velocity (i.e., reversed flow) The figure clearly shows a core of reversed flow embedded within the computational domain. The center of the core is located on neither the $\phi = 0°$ nor the $\phi = 30°$ plane. No reverse flow occurs anywhere in the computed flow field downstream from the most downstream plane in the figure.

Figure 24 shows computed crossflow velocity vectors for Solution 3-B within a cross-sectional plane downstream from the base. This plane is located approximately 3/8 cal downstream from the base and corresponds to the fourth downstream plane from the base shown in the previous figure. The plot includes a shaded area which provides a magnified view of the reversed flow region from the previous figure. At this axial location, it is apparent that the crossflow direction within the reverse flow region is primarily outward from the axis, while the crossflow direction elsewhere is primarily inward toward the axis.

7. CONCLUSION

A CFD study of finned KE projectile base flow has been presented for supersonic flight conditions. A parabolized Navier-Stokes technique was used to compute the attached flow over the forebody and fins; an unsteady Navier-Stokes technique was used to compute the flow in the base region. Several CFD solutions for free stream Mach numbers 3, 4, and 5 were presented, and the modeling approach and computational requirements were discussed. The computed zero-yaw drag was compared to range-acquired values, and the flow structure was briefly examined.

The numerical solutions used computer times on the order of hundreds of hours on a Cray X-MP computer. The largest solution, which had a six-fold increase in the number of grid points (more than 600,000) compared to the others, used more than 1000 hours on a Cray-2 computer. All of the solution data sets are valuable, not only because they represent a considerable investment of resources, but also because they provide superior initial conditions for future CFD work in this area.

While the present two-zone approach provides a good starting point for the problem, a multiple zone strategy would provide more flexibility, especially for more complex config-urations (such as those with overhanging fins, for example). As discussed within, several aspects of the CFD results strongly suggest that a further increase in grid resolution may be required to resolve the flow structures in certain regions of the flow field.

19

The computed zero-yaw drag of the projectile was shown to underpredict the range-acquired drag by about 9% at Mach 3 and 5% at Mach 4. The many modeling simplifications used in the current CFD approach which could contribute to differences between the computed and range-acquired drag were discussed. Though the drag comparison serves as an initial indicator of the accuracy of the CFD approach, it is concluded that precise validation of finned projectile base flow CFD modeling should focus on wind tunnel base and fin trailing edge pressure measurements. Future work in this area should also include the investigation of finless models.

Overall, the computed base flow structure is shown to exhibit complex, fully 3-D features. No axisymmetry exists within the cylinder base region, and the base flow structure is quite different from that of axisymmetric base configurations that have been reported to date. It is conceded that uncertainty remains concerning the adequacy of the current grid resolution and modeling simplifications. Much of this uncertainty is driven by the lack of sufficient computational power needed to conduct parametric studies that address these issues. The current facilities, while having enough core memory, provide insufficient CPU time per user to allow such an investigation to be promptly conducted. The study presented here serves as a stepping-stone for future CFD modeling that should eventually lead to a capability for predicting, understanding, and controlling KE projectile base flow.
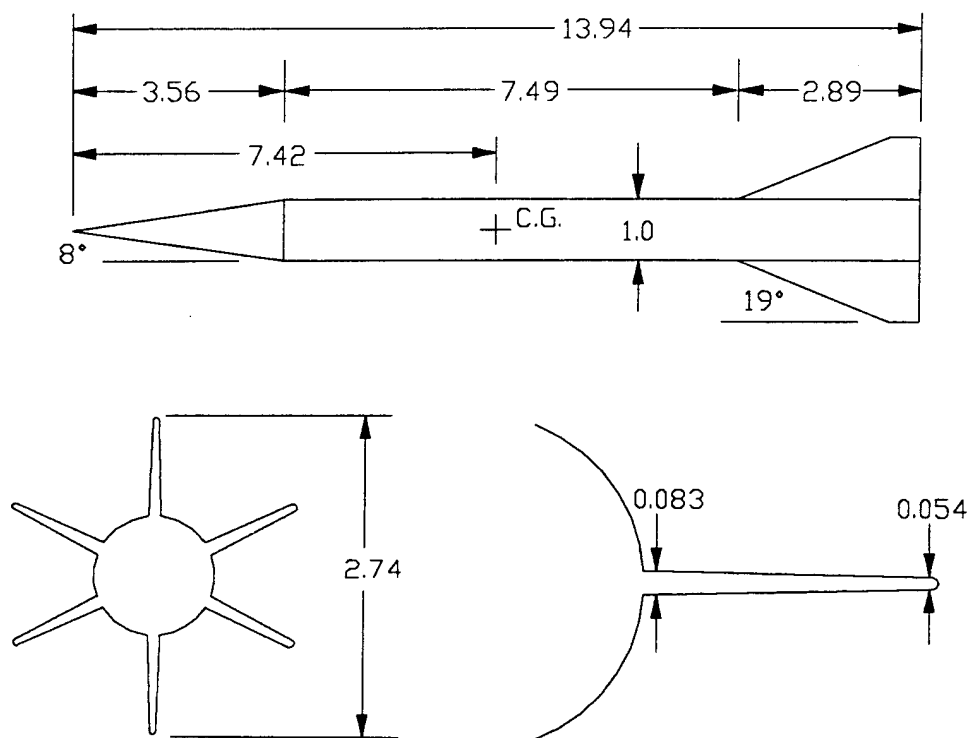
All Dimensions in Calibers (One Caliber=35.2 mm)

Figure 1. M735 Projectile Model

Figure 2. Roll Angle, ϕ

KE PROJECTILE BASE FLOW MODELING

Parabolized
Navier-Stokes
Domain

Unsteady
Navier-Stokes
Domain

Overlapping
Zonal
Boundaries

Zone 1

Zone 2
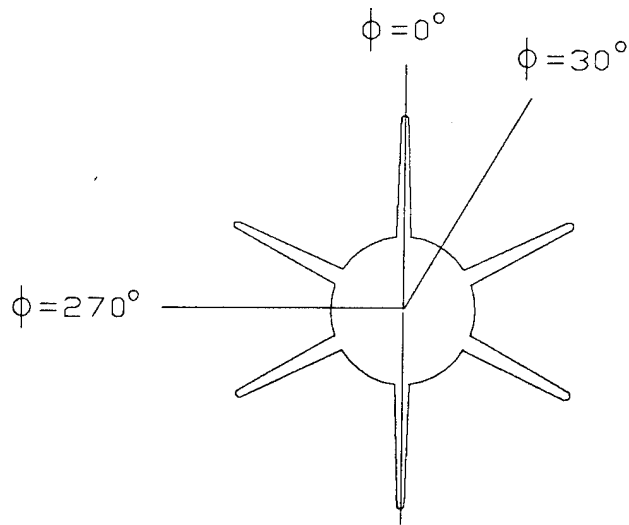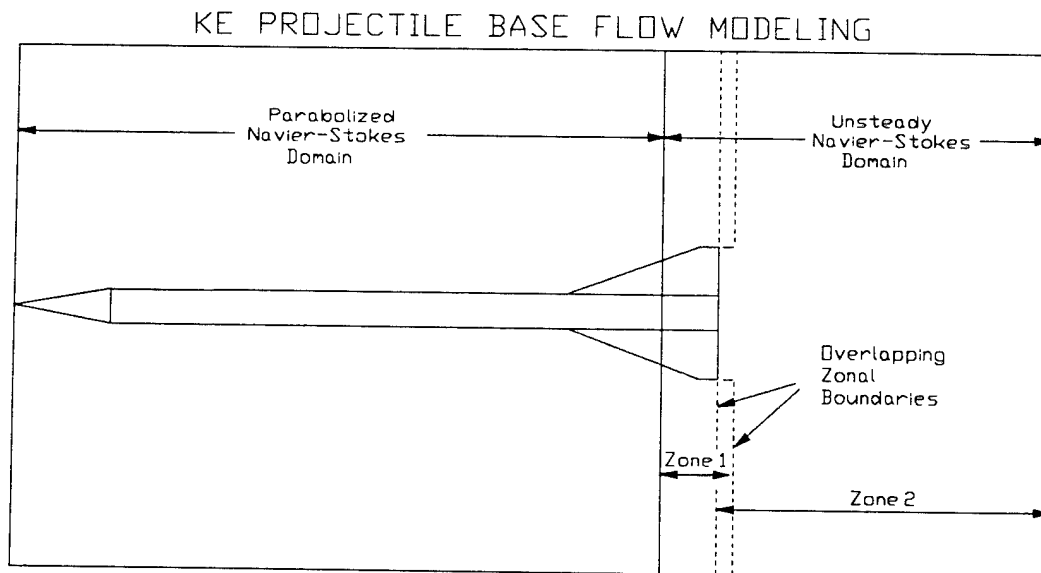
Figure 3. Code Coupling for Finned Projectile Base Flow Modeling, $\phi = 0°$
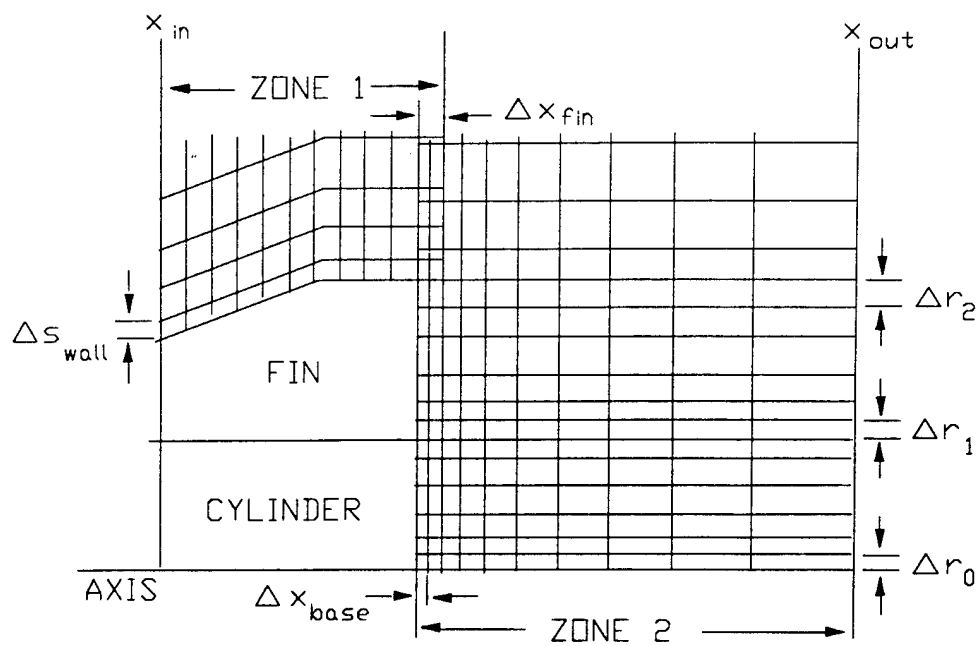
Figure 4. Grid Parameters for Finned Projectile Base Flow Modeling
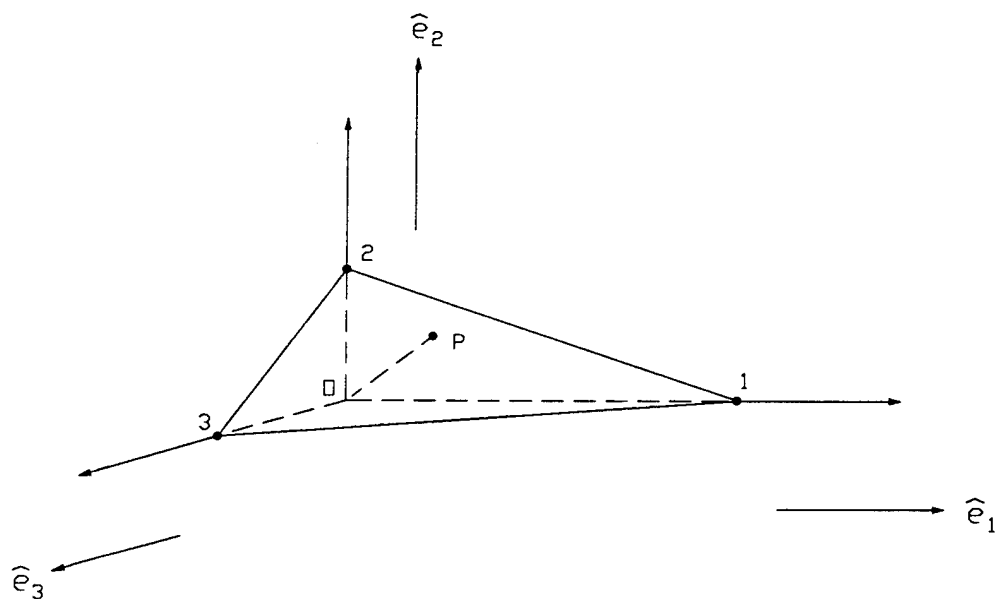
Figure 5. Zonal Boundary Interpolation Scheme

23
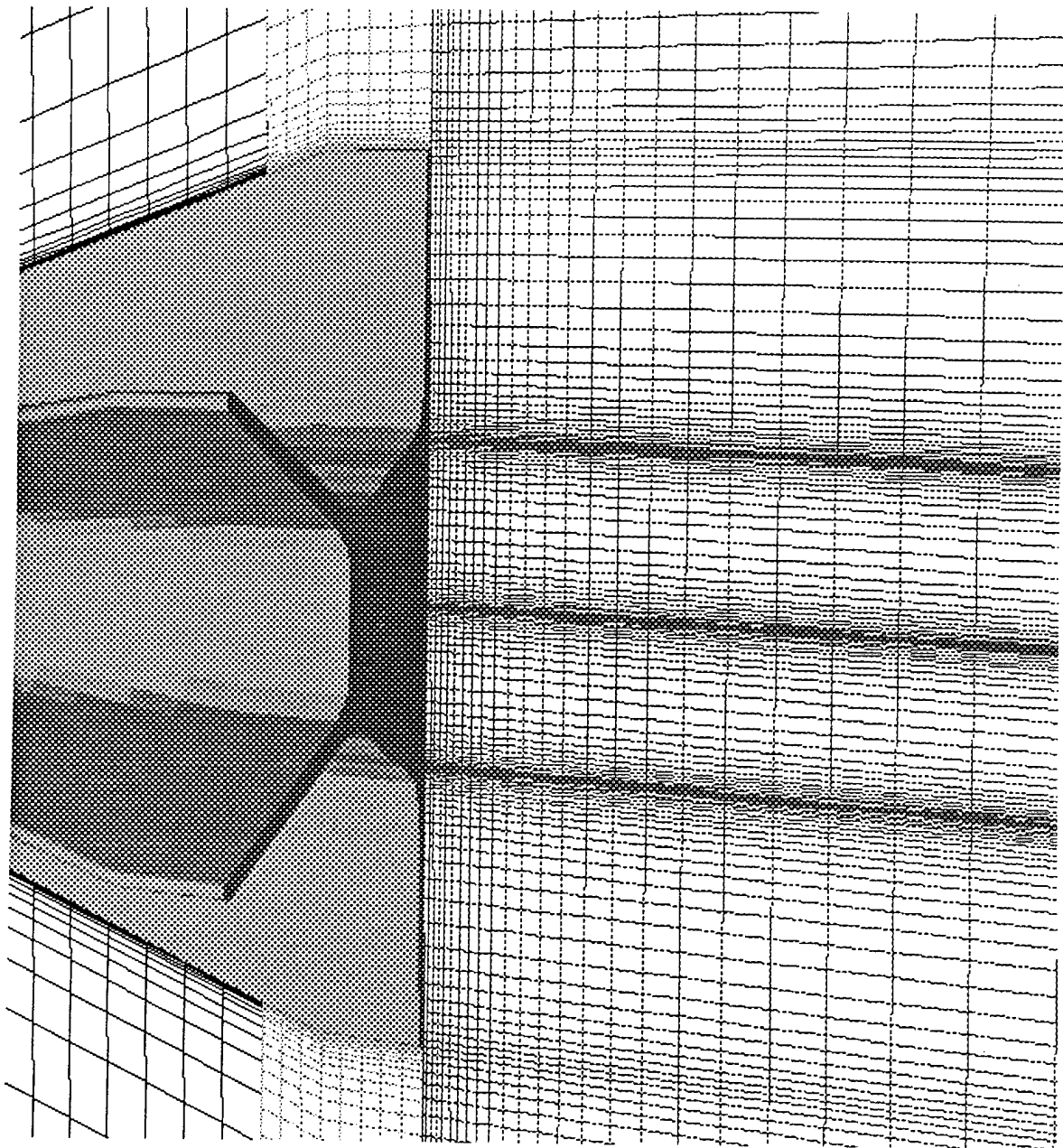
Figure 6. Side View of Grid 4-C, $\phi = 0°$
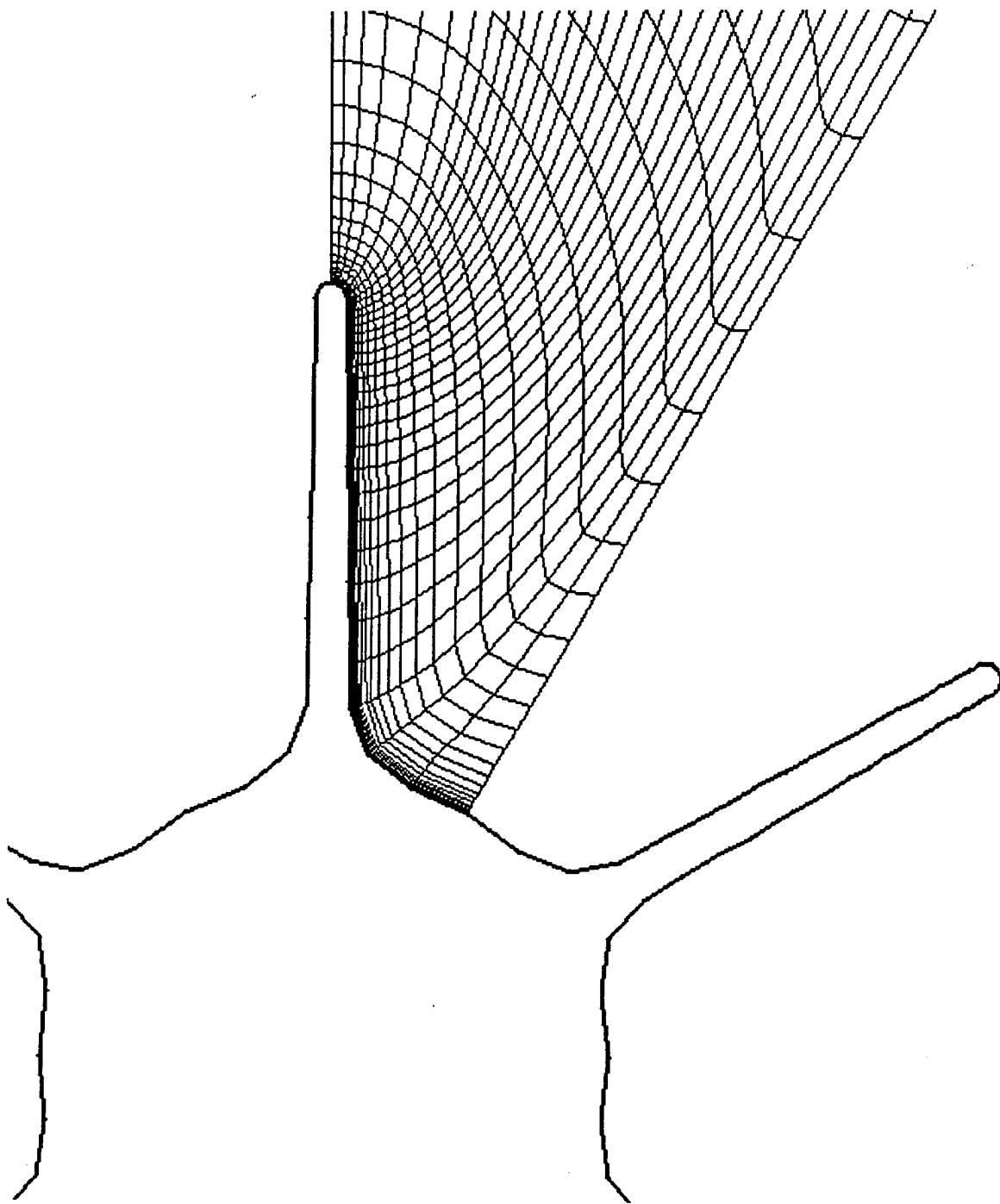
Figure 7. Cross-Sectional View of Grid 3-B, Zone 1, x/d=13.94
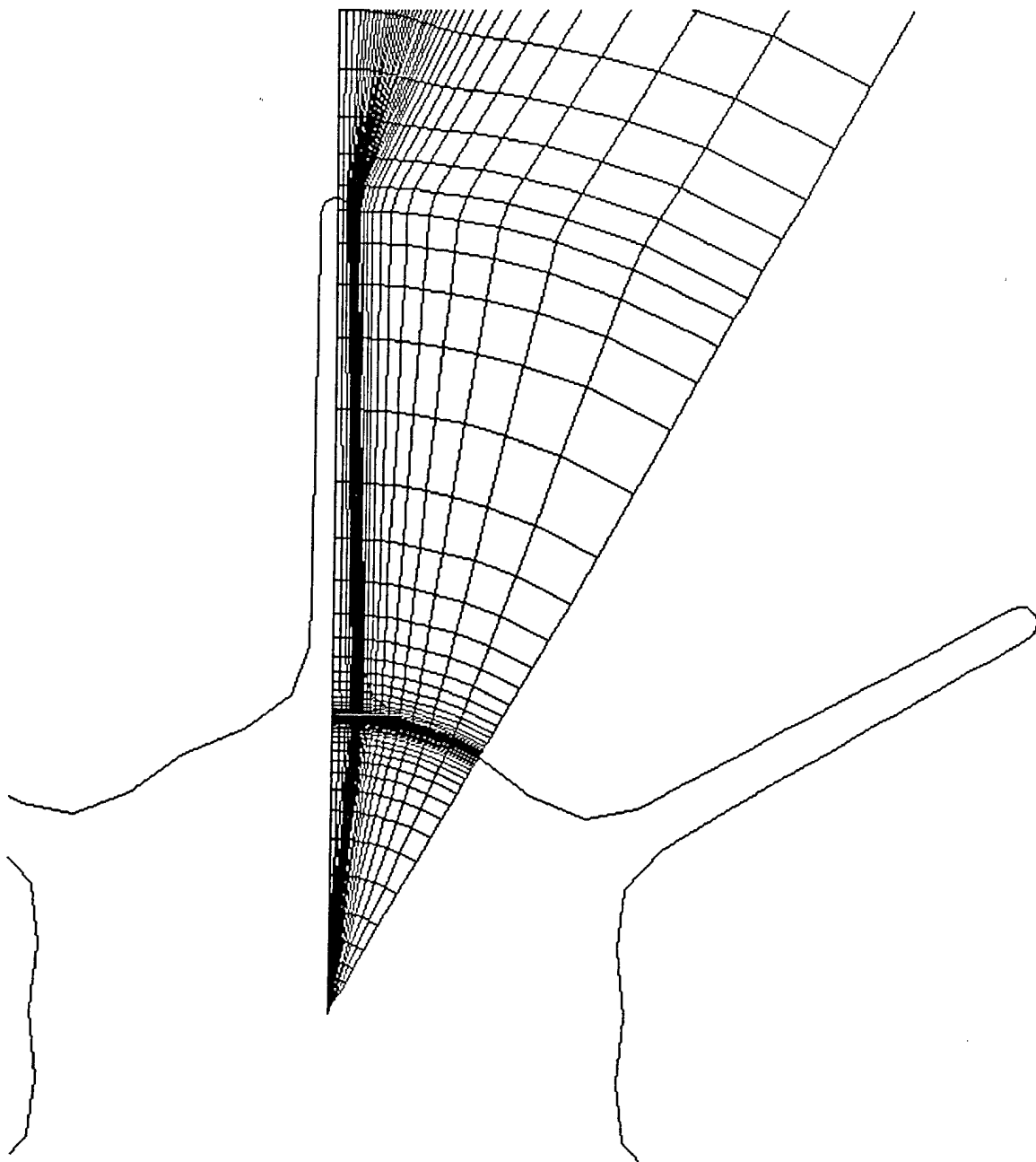
Figure 8. Cross-Sectional View of Grid 3-B, Zone 2, x/d=13.94
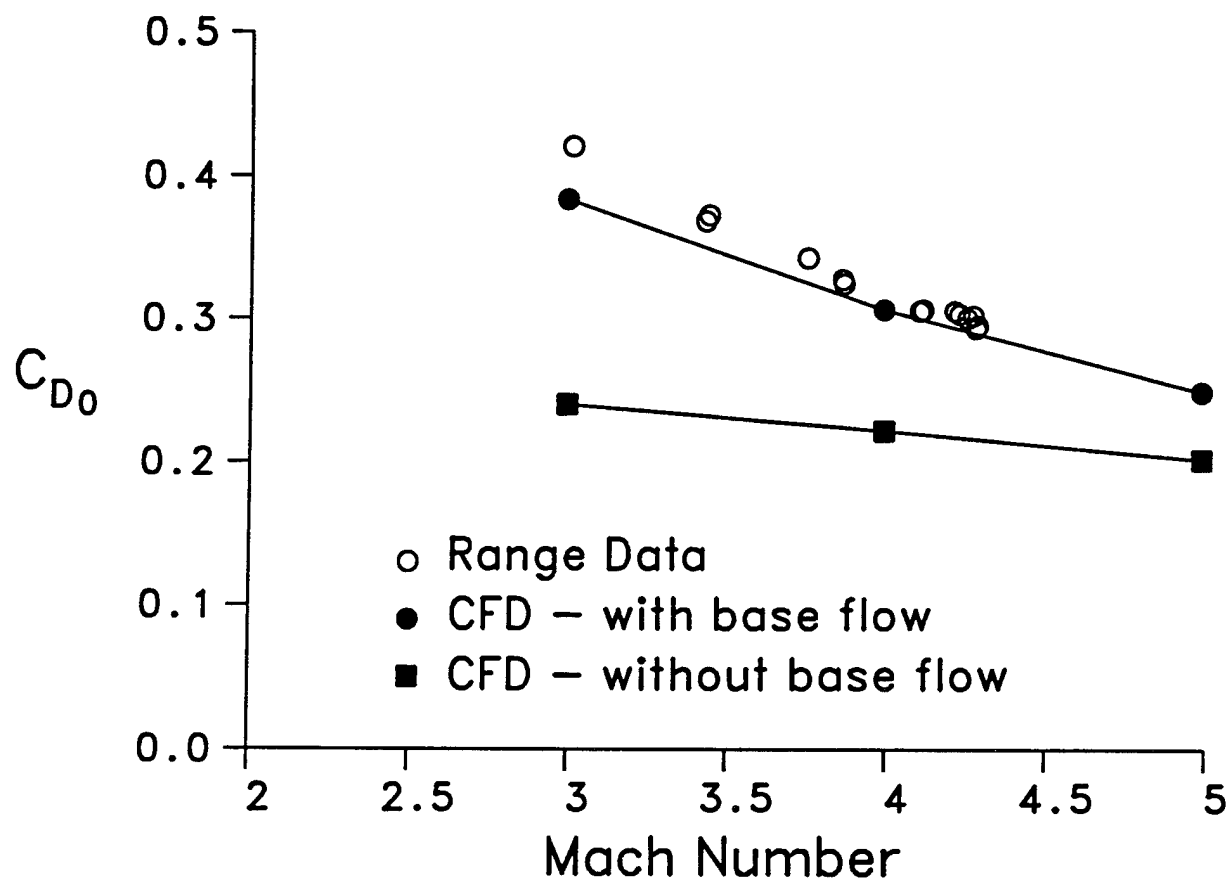
Figure 9. Comparison of Computed and Range-Acquired Zero-Yaw Drag Coefficients
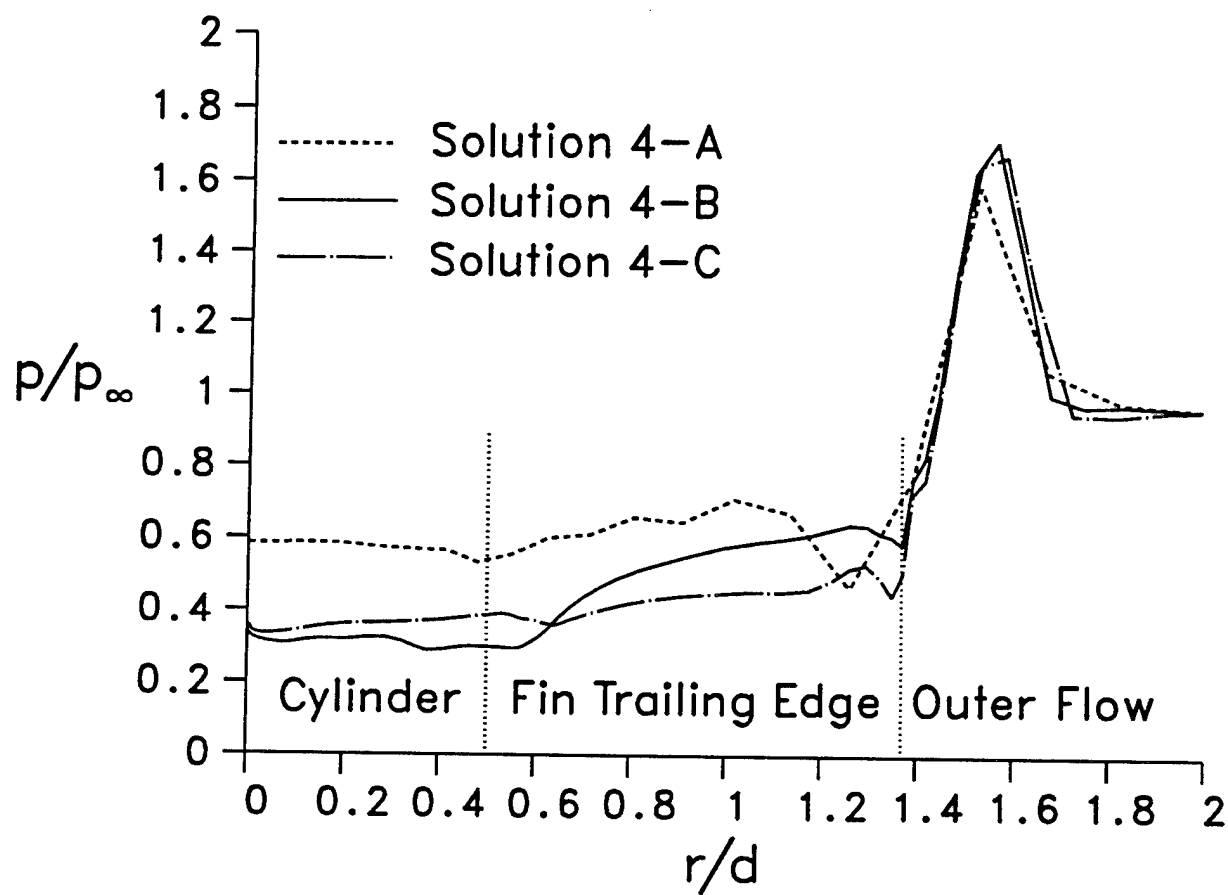
Figure 10. Computed Base Pressures, $M_\infty = 4$, $\phi = 0°$
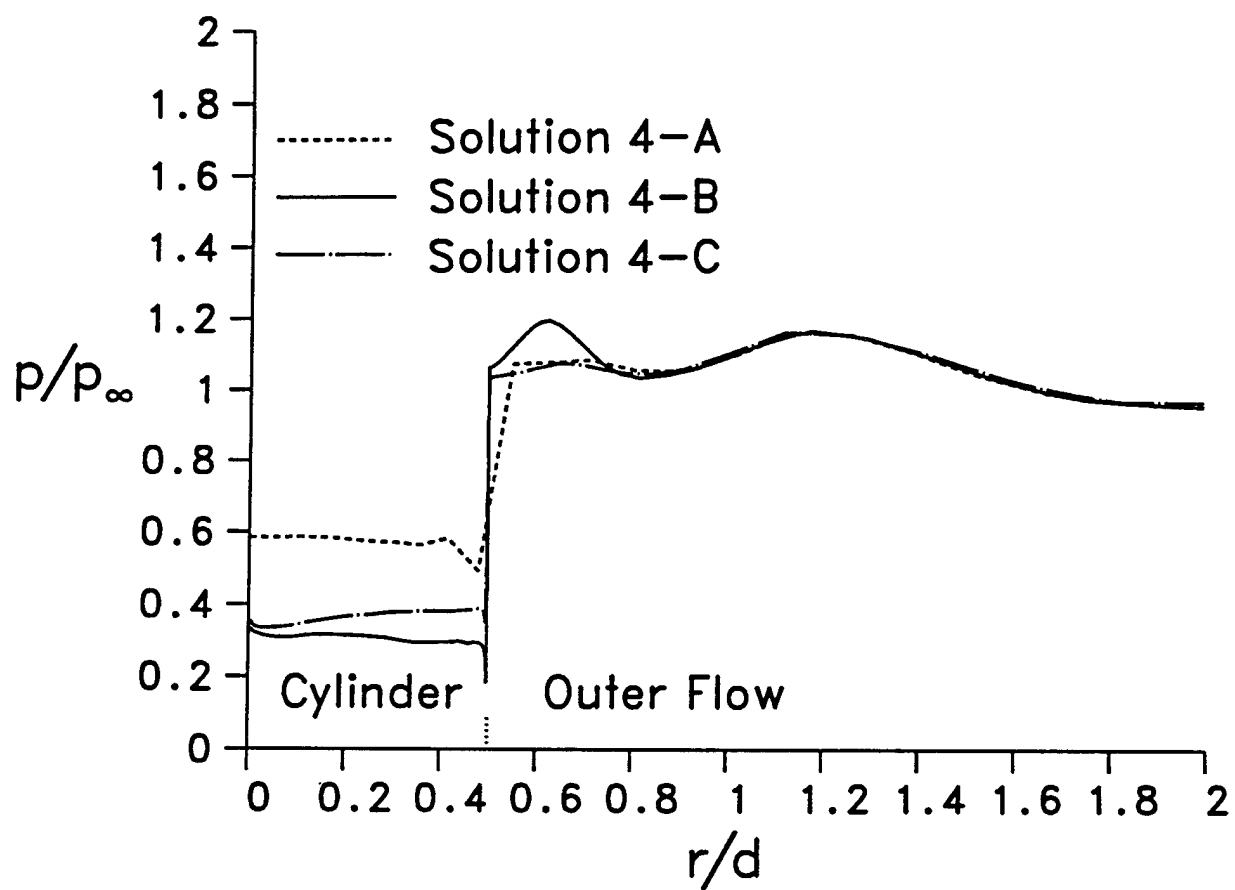
Figure 11. Computed Base Pressures, $M_\infty = 4$, $\phi = 30°$
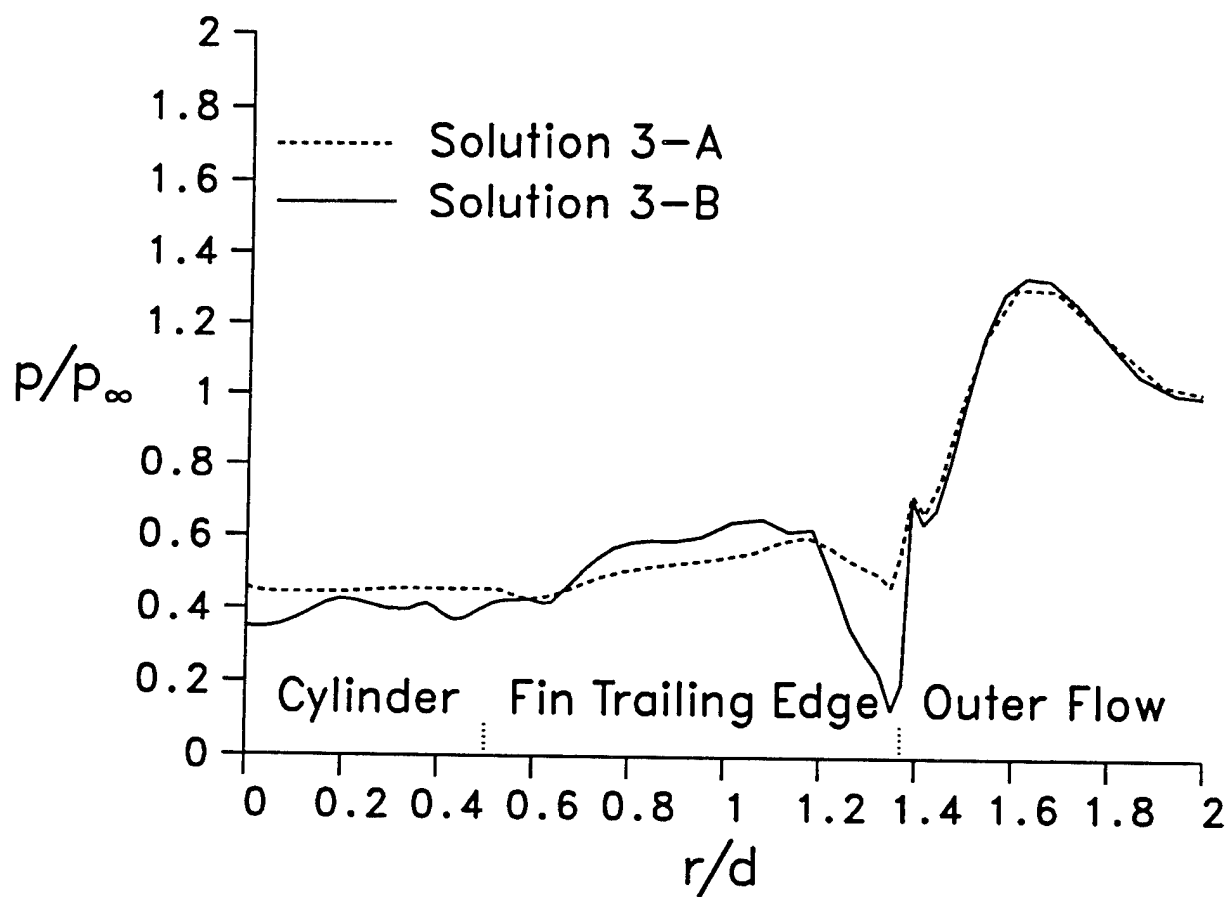
Figure 12. Computed Base Pressures, $M_\infty = 3$, $\phi = 0°$
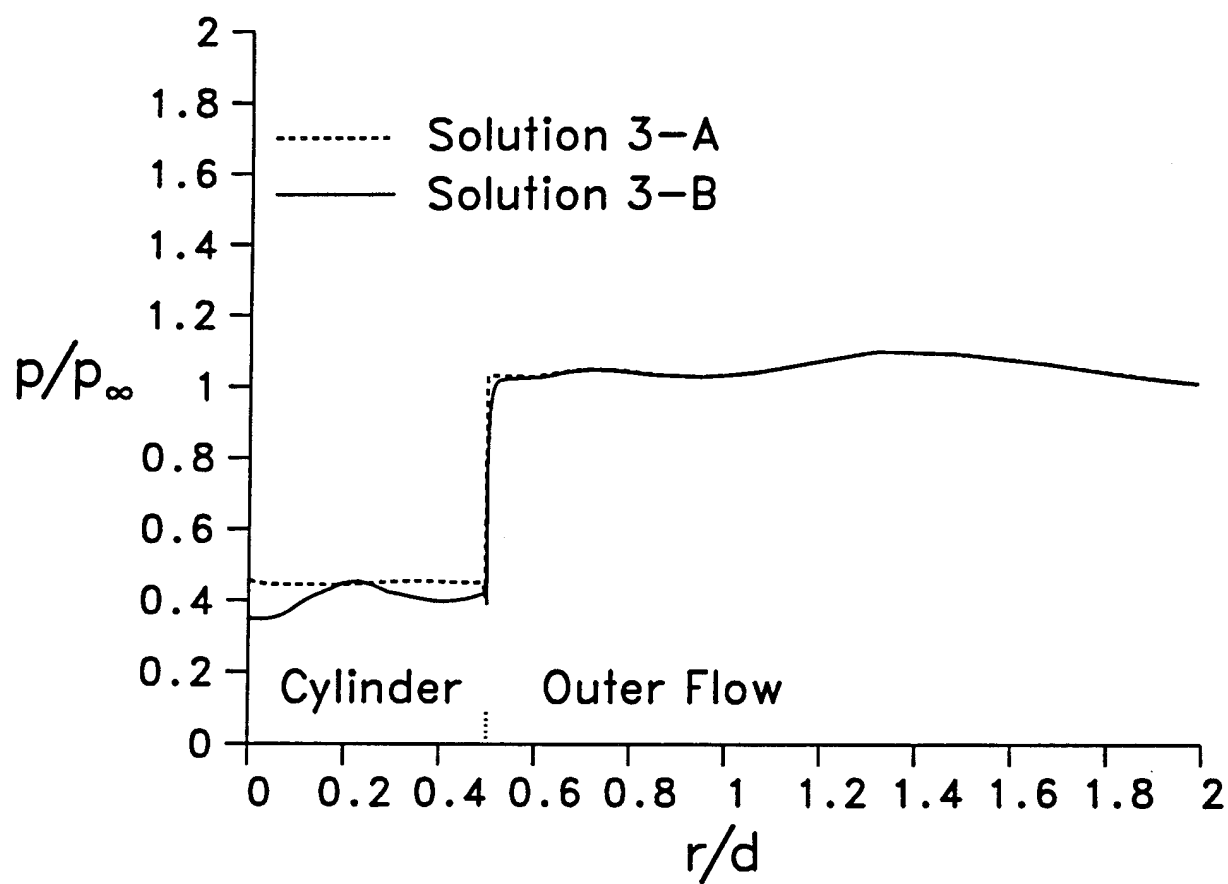
Figure 13. Computed Base Pressures, $M_\infty = 3$, $\phi = 30°$
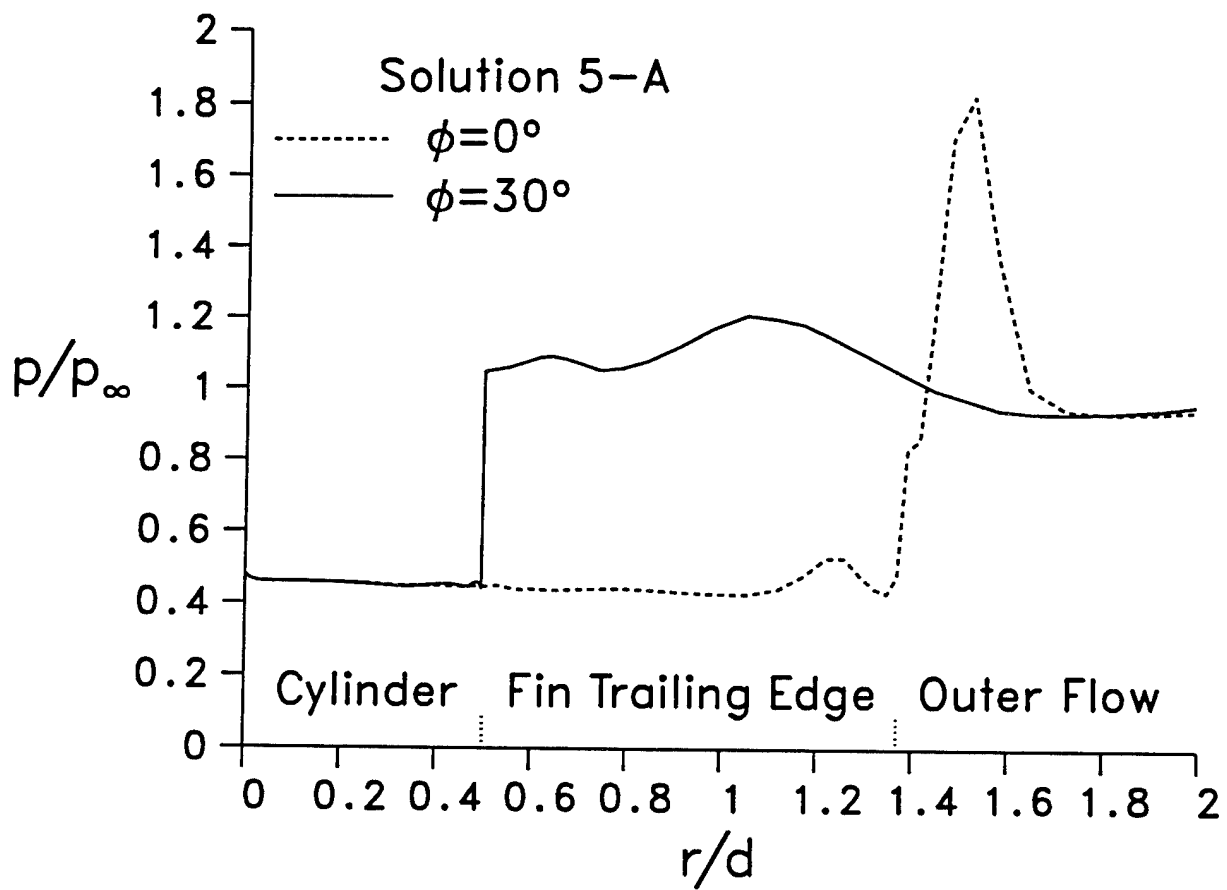
Figure 14. Computed Base Pressures, $M_\infty = 5$, $\phi = 0°$ and $\phi = 30°$
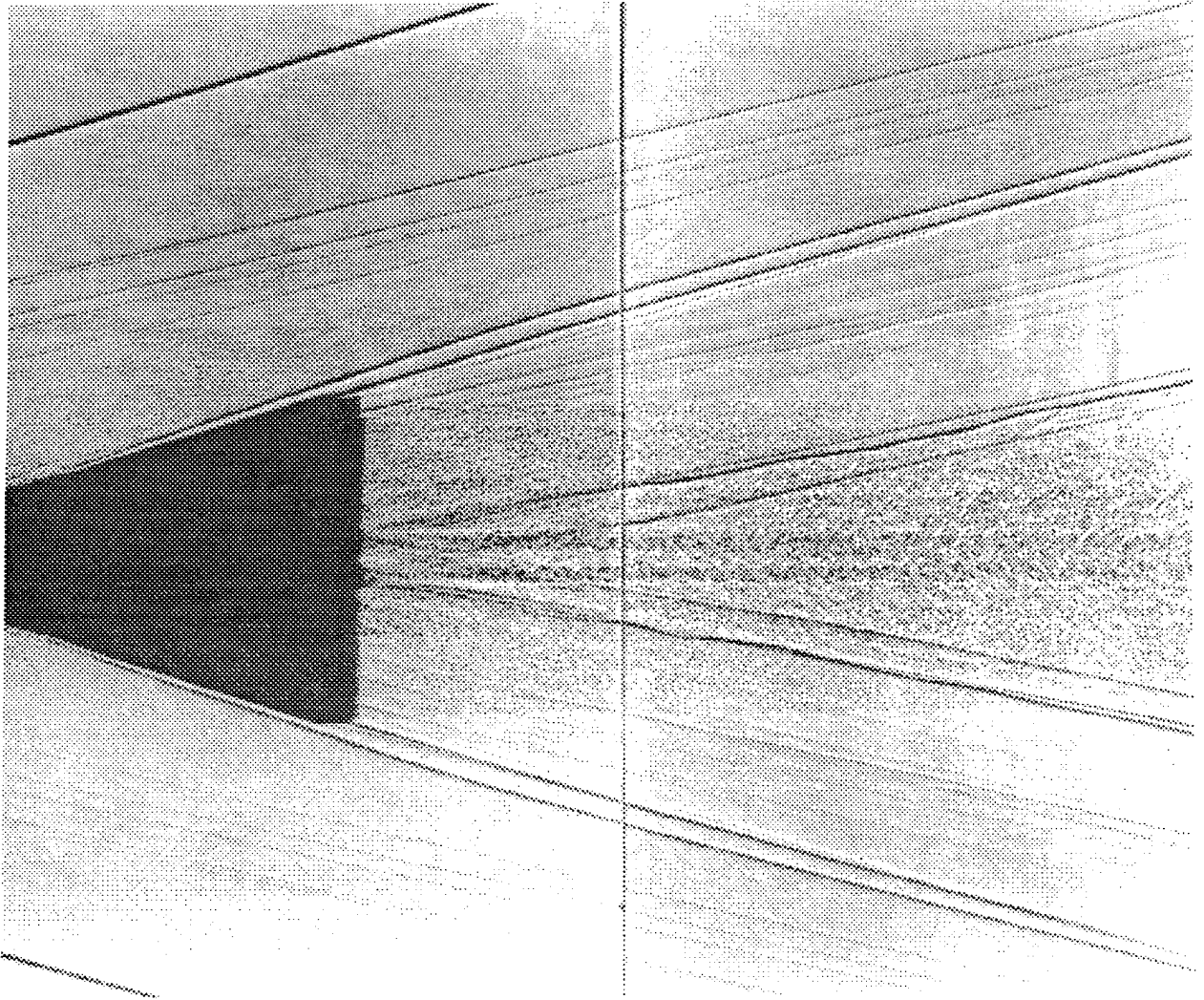
Figure 15. M735 Shadowgraph, $M_\infty = 4.3$
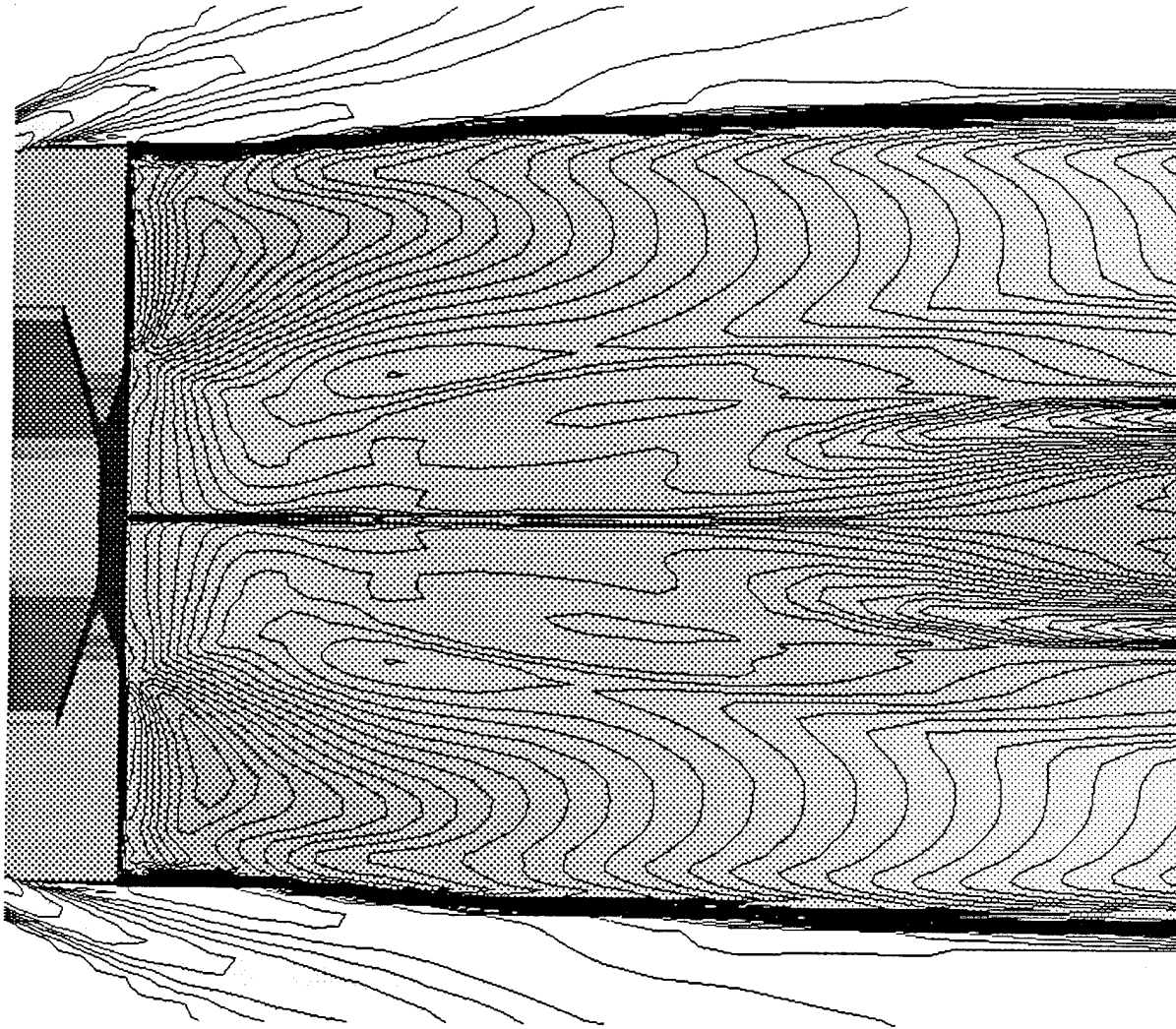
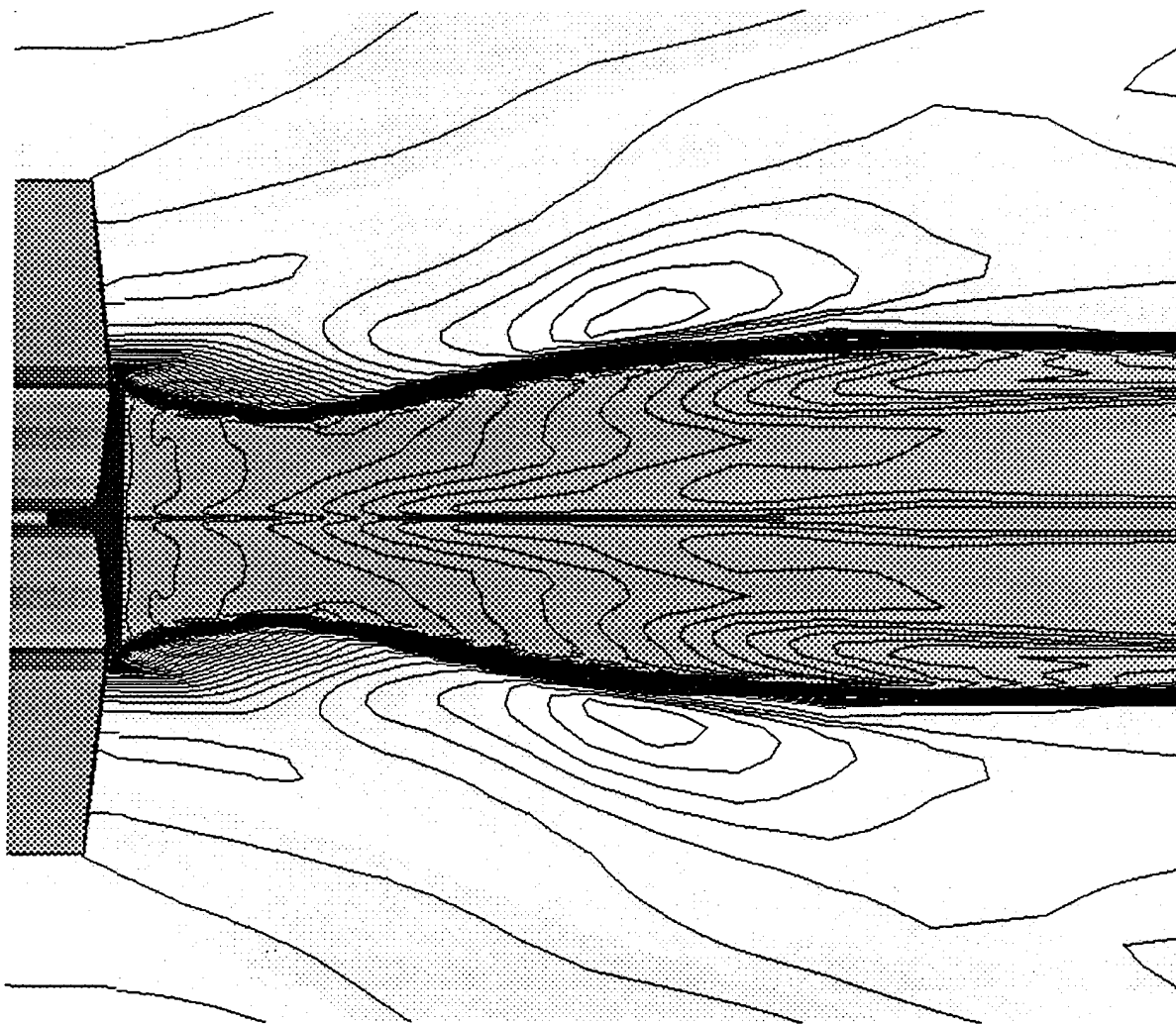**Figure 16.** Mach Contours (0.0 to 4.2 in 0.1 increments), $M_\infty = 4$ (Solution 4-C), $\phi = 0°$

Figure 17. Mach Contours (0.0 to 4.6 in 0.1 increments), $M_\infty = 4$ (Solution 4-C), $\phi = 30°$

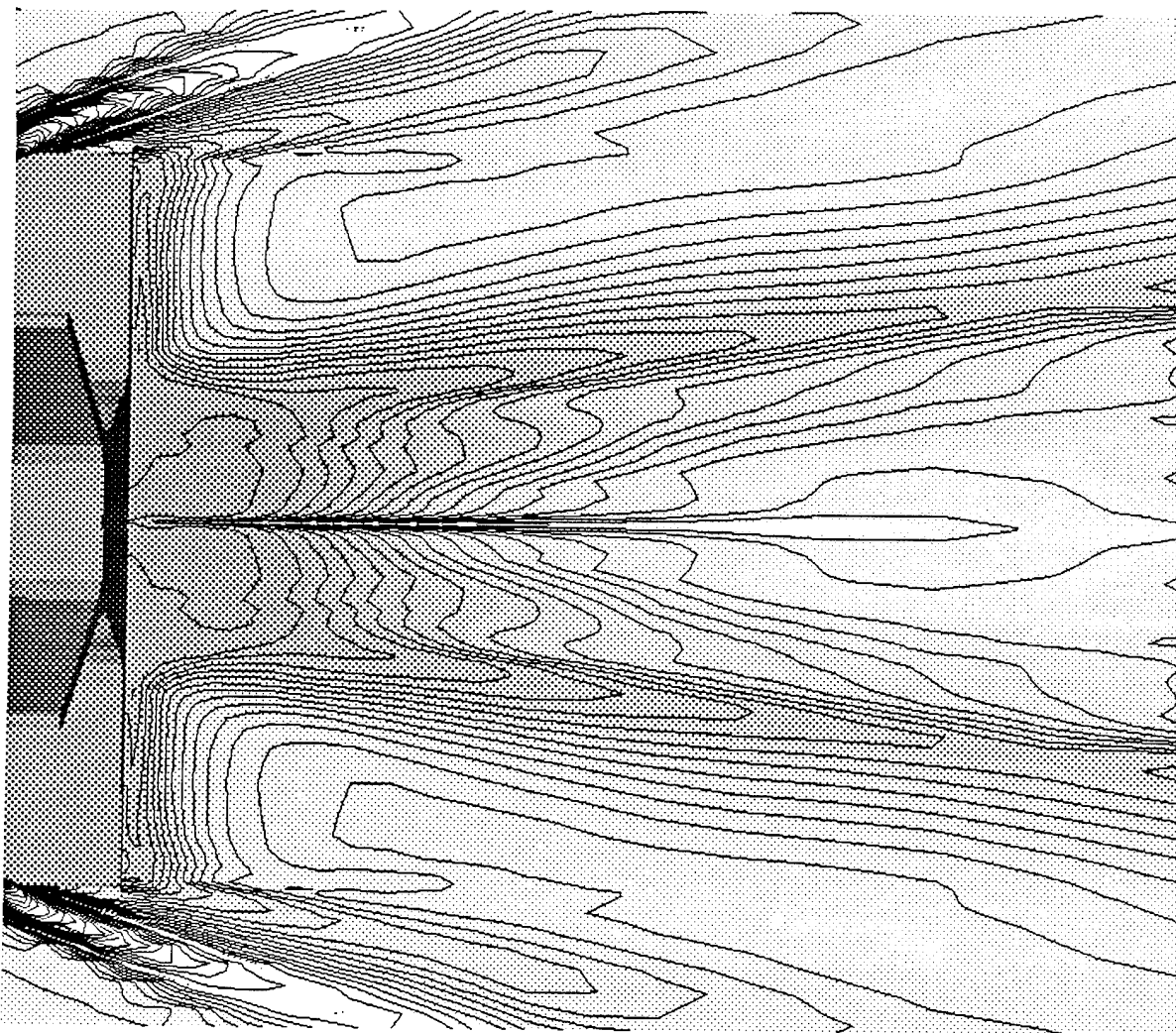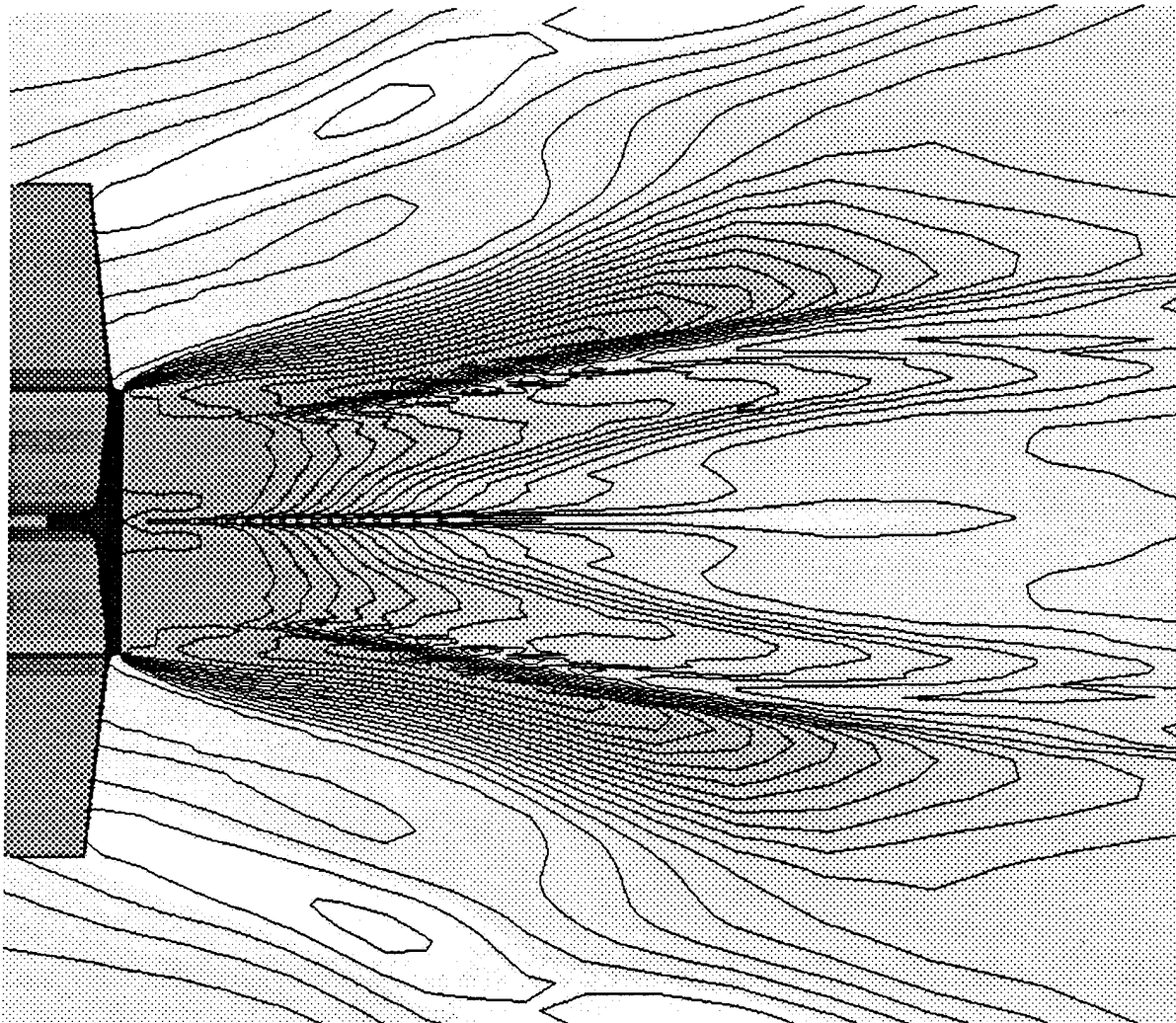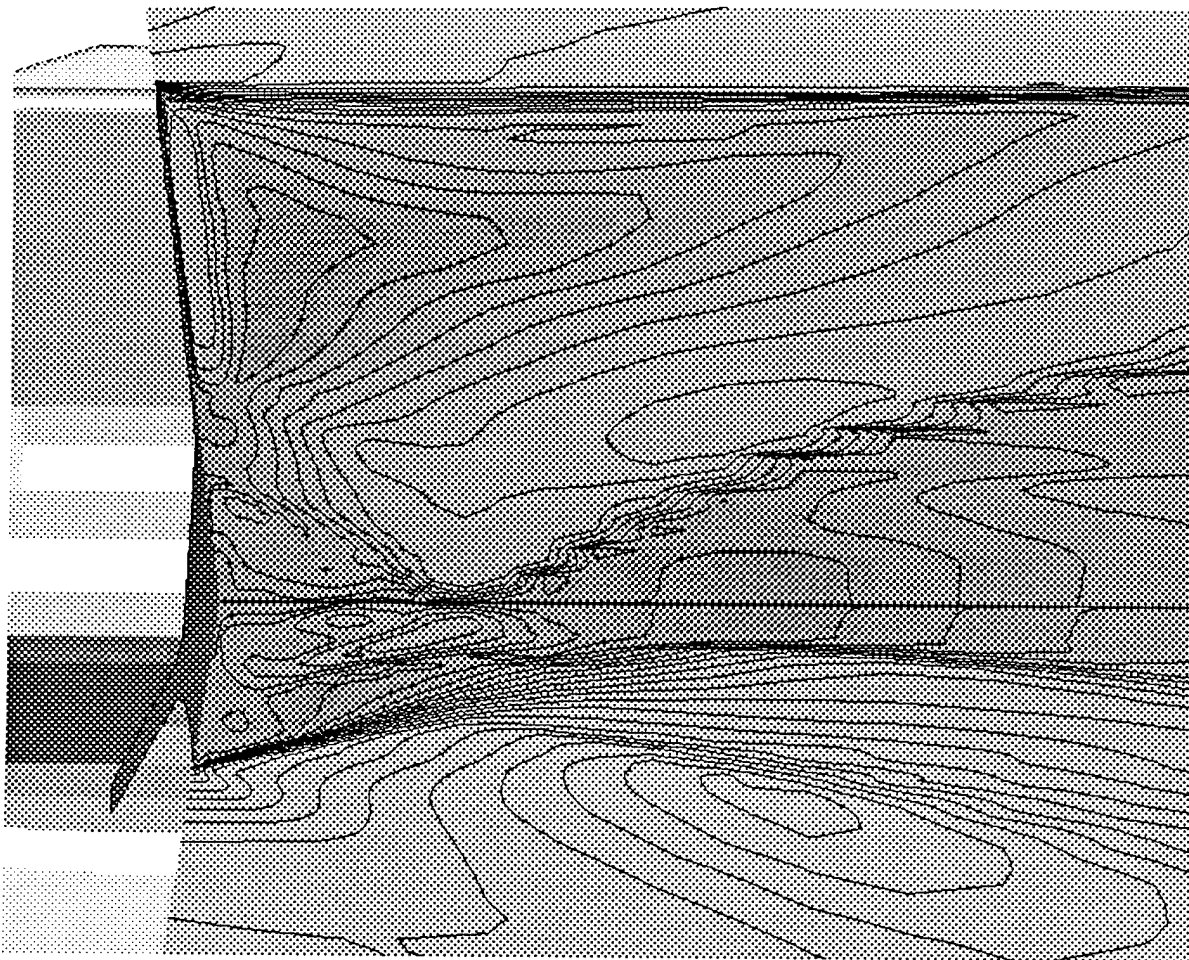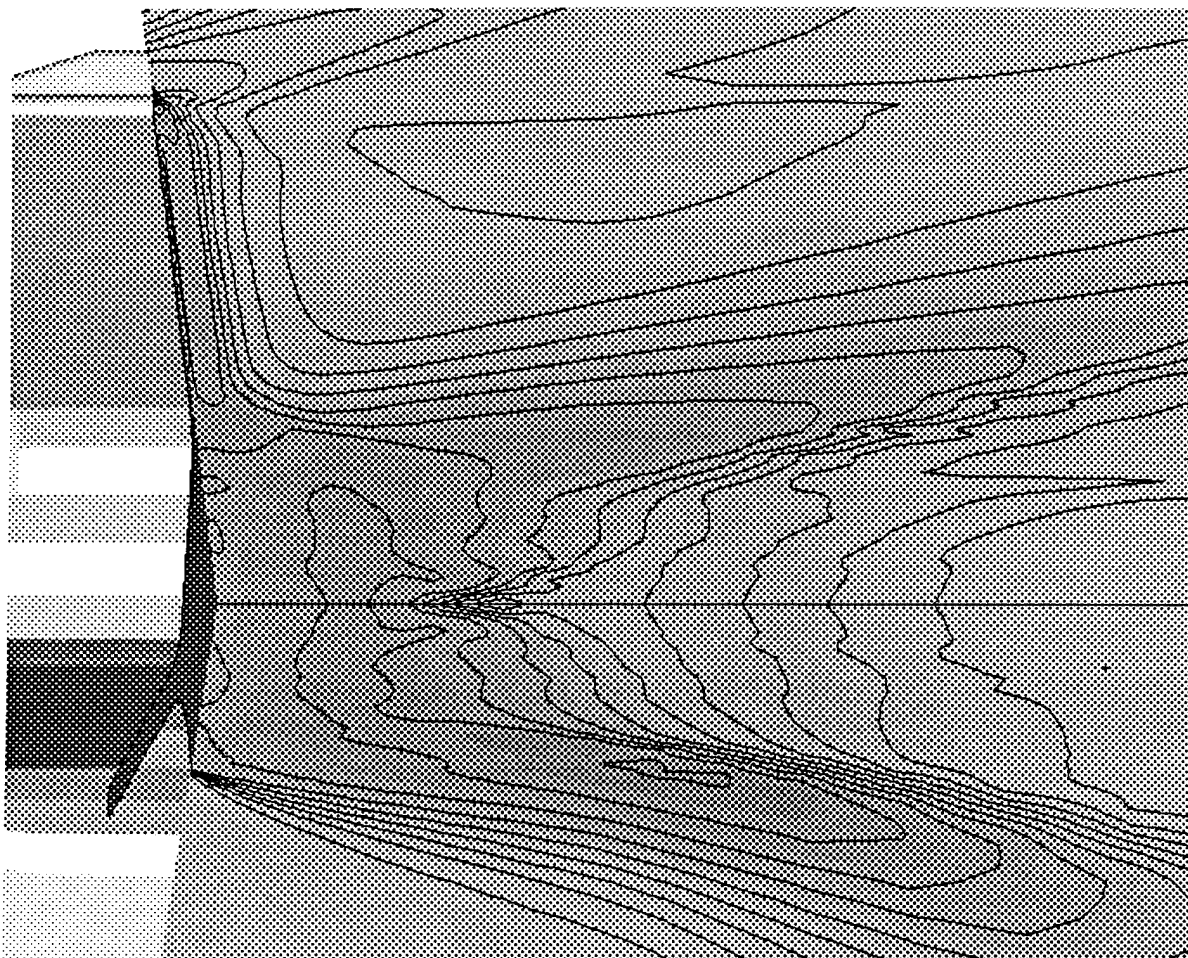**Figure 18.** p/p_∞ Contours (0.25 to 4.0 in 0.05 increments), $M_\infty = 4$ (Solution 4-C), $\phi = 0°$

36

Figure 19. p/p_∞ Contours (0.25 to 1.3 in 0.05 increments), $M_\infty = 4$ (Solution 4-C), $\phi = 30°$

Figure 20. Mach Contours (0.0 to 4.0 in 0.2 increments), $M_\infty = 3$ (Solution 3-B), $\phi = 0°$ and $\phi = 30°$

Figure 21. p/p_∞ Contours (0.15 to 1.2 in 0.05 increments), $M_\infty = 3$ (Solution 3-B), $\phi = 0°$ and $\phi = 30°$

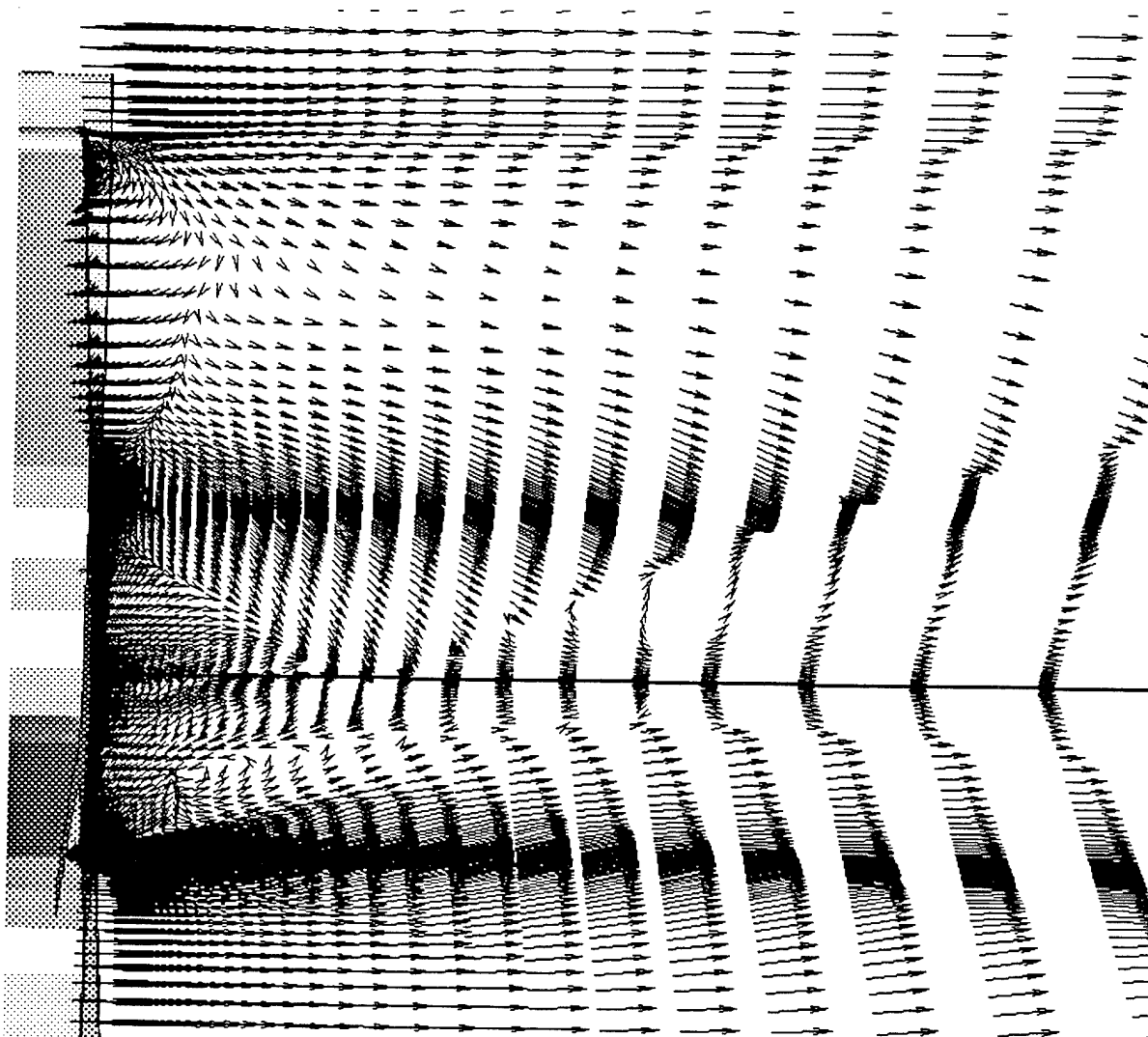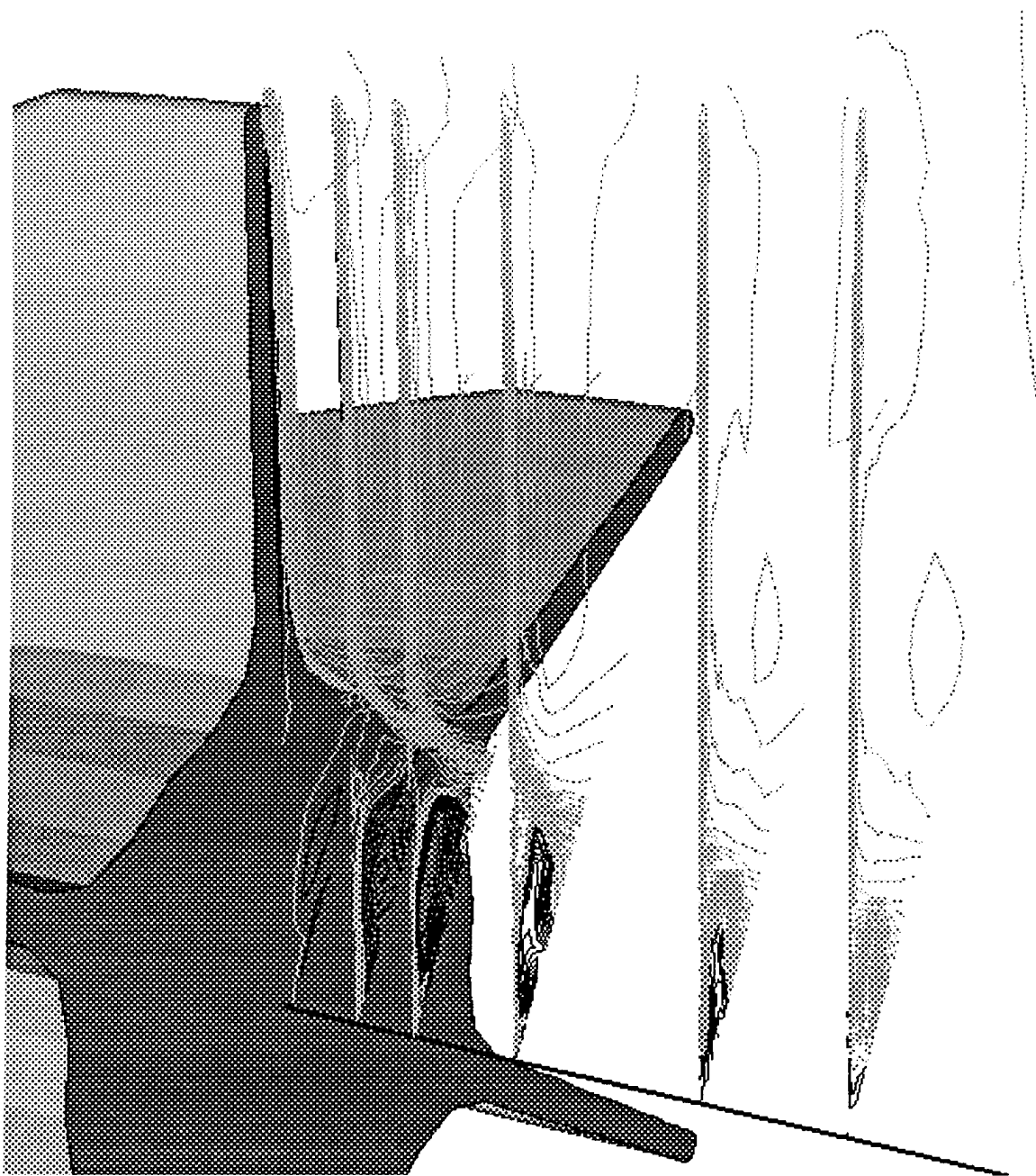**Figure 22.** Velocity Vectors, $M_\infty = 3$ (Solution 3-B), $\phi = 0°$ and $\phi = 30°$

40

Figure 23. u/a_∞ Contours (-1.4 to 4.0 in 0.2 increments), $M_\infty = 3$ (Solution 3-B), at Six Axial Locations

Figure 24. Crossflow Velocity Vectors, $M_\infty = 3$ (Solution 3-B), $x/d = 14.6$

8. REFERENCES

Baldwin, B., and H. Lomax, "Thin-Layer Approximation and Algebraic Model for Separated Turbulent Flows," AIAA Paper No. 78-0257, January 1978.

Beam, R., and R. Warming, "An Implicit Factored Scheme for the Compressible Navier-Stokes Equations," AIAA Journal, Vol. 16, No. 4, pp. 393-402, 1978.

Berner, C., C. Demeautis, and P. Duffner, "Vol de deux projectiles separes par une faible distance. I.1: Visualisation des ecoulements et mesures de pression autour de projectiles de reference," Rapport R 107/92, Institut Franco-Allemand deRecherches de Saint-Louis, France, May 1992.

Chakravarthy, S., and S. Osher. "High Resolution Applications of the Osher Upwind Scheme for the Euler Equations," AIAA Paper No. 83-39390, 1983.

Edwards, T., "The Effect of Exhaust Plume/Afterbody Interaction on Installed Scramjet Performance," NASA Technical Memorandum 101033, Ames Research Center, Moffett Field, California, December 1988.

Edwards, T., D. Chaussee, S. Lawrence, and Y. Rizk, "Comparisons of Four CFD Codes as Applied to a Hypersonic All-Body Vehicle," AIAA Paper No. 87-2642, August 1987.

Guidos, B., "Static Aerodynamics CFD Analysis for 120-mm Hypersonic KE Projectile Design," ARL-MR-184, U.S. Army Research Laboratory, Aberdeen Proving Ground, Maryland, September 1994. (AD A285471)

Guidos, B., and P. Weinacht, "Parabolized Navier-Stokes Computation of Surface Heat Transfer Characteristics for Supersonic and Hypersonic KE Projectiles," ARL-TR-191, U.S. Army Research Laboratory, Aberdeen Proving Ground, Maryland, August 1993. (AD A268858)

Mikhail, A., "Drag Correlation and Predictions of Surface Groove Drag for Kinetic Energy Projectiles," Journal of Spacecraft and Rockets, Vol. 26, No. 5, pp.308-313, September-October 1989.

Moore, F., and T. Hymer, "Base Drag Prediction on Missile Configurations," AIAA Paper No. 93-3629, 1993.

Murphy, C., "Free Flight Motion of Symmetric Missiles," Ballistic Research Laboratories Report No. 1216, Aberdeen Proving Ground, MD, July 1963. (AD 442757)

Pulliam, T., and J. Steger, "On Implicit Finite-Difference Simulations of Three-Dimensional Flow," AIAA Paper No. 78-0019, January 1978.

Rai, M., "Three-Dimensional Navier-Stokes Simulations of Turbine Rotor-Stator Interaction; Part I - Methodology," Journal of Propulsion and Power, Vol. 5, No. 3, pp. 305-311, 1989.

Rai, M., and S. Chakravarthy, "An Implicit Form for the Osher Upwind Scheme," AIAA Journal, Vol. 24, No. 5, pp. 735-743, 1986.

Rai, M., and D. Chaussee, "New Implicit Boundary Procedures: Theory and Applications," AIAA Paper No. 83-0123, January 1983.

Rai, M., D. Chaussee, and Y.M. Rizk, "Calculation of Viscous Supersonic Flows Over Finned Bodies," AIAA Paper No. 83-1667, July 1983.

Sturek, W., L. Kayser, and D. Mylin, "Boundary-Layer Trip Effectiveness and Computations of Aerodynamic Heating for XM797 Nose-Tip Configurations," ARBRL-MR-03262, U.S. Army Ballistic Research Laboratory, Aberdeen Proving Ground, Maryland, April 1983. (AD A128036)

Schiff, L., and J. Steger, "Numerical Simulation of Steady Supersonic Flow," AIAA Paper No. 79-0130, January 1979.

Steger, J., "Implicit Finite-Difference Simulation of Flow about Two-Dimensional Bodies," AIAA Journal, Vol. 16, No. 7, pp.679-686, 1978.

Sturek, W., L. Kayser, D. Mylin, "Boundary-Layer Trip Effectiveness and Computations of Aerodynamic Heating for XM797 Nose-Tip Configurations," ARBRL-MR-03262, U.S. Army Ballistic Research Laboratory, Aberdeen Proving Ground, Maryland, April 1983. (AD A128036)

Sturek, W., C. Nietubicz, J. Sahu, and P. Weinacht, "Recent Applications of CFD to the Aerodynamics of Army Projectiles," ARL-TR-22, U.S. Army Research Laboratory, Aberdeen Proving Ground, Maryland, December 1992. (AD A262953)

Sturek, W., and L. Schiff, "Computations of the Magnus Effect for Slender Bodies in Supersonic Flow," ARBRL-TR-02384, U.S. Army Ballistic Research Laboratory, Aberdeen Proving Ground, Maryland, December 1981. (AD A110016)

Weinacht, P., B. Guidos, L. Kayser, and W. Sturek, "PNS Computations for Spinning and Fin-Stabilized Projectiles at Supersonic Speeds," ARBRL-MR-3464, U.S. Army Ballistic Research Laboratory, Aberdeen Proving Ground, Maryland, September 1985. (AD A160393)

Weinacht, P., B. Guidos, W. Sturek, and B. Hodes, "PNS Computations for Spinning Shell at Moderate Angles of Attack and for Long L/D Finned Projectiles," BRL-MR-3522, U.S. Army Ballistic Research Laboratory, Aberdeen Proving Ground, Maryland, June 1986. (AD 169531)

Weinacht, P., and W. Sturek, "Computation of the Roll Characteristics of Finned Projectiles," BRL-TR-2931, U.S. Army Ballistic Research Laboratory, Aberdeen Proving Ground, Maryland, June 1988. (AD 197875)

Weinacht, P., and W. Sturek, "Navier-Stokes Predictions of Pitch Damping for Finned Projectiles Using Steady Coning Motion," AIAA Paper 90-3088, August 1990.

Weinacht, P., W. Sturek, and L. Schiff, "Navier-Stokes Predictions of Pitch Damping for Axisymmetric Shell Using Steady Coning Motion," AIAA Paper 91-2855, August 1991.

LIST OF SYMBOLS

$\tilde{A}\pm, \tilde{B}\pm, \tilde{C}\pm$	flux-split Jacobian matrices of transformed inviscid flux vectors
a	speed of sound
C_D	total drag coefficient
C_{D_O}	zero-yaw drag coefficient
C_{D_B}	base and fin trailing edge drag coefficient
C_{D_F}	forebody and fin attached flow drag coefficient
$C_{D_{\delta^2}}$	yaw drag coefficient
d	projectile reference diameter
$\tilde{E}, \tilde{F}, \tilde{G}$	inviscid flux vectors of transformed gas dynamic equations
$\hat{E}, \hat{F}, \hat{G}$	first order numerical inviscid flux vectors of transformed gas dynamic equations
I	identity matrix
i, j, k	grid indices in ξ, η, ζ directions
J	Jacobian of coordinate transformation
L	unit length
M	Mach number
N	Jacobian matrix of viscosity terms in ζ direction
P_r	Prandtl number for laminar flow
p	pressure
$\bar{Q}$	vector of dependent variables of gas dynamic equations
$\tilde{Q}$	transformed vector of dependent variables of gas dynamic equations
q	dynamic pressure
R_e	Reynolds number, $\rho_\infty u_\infty L / \mu_\infty$
$\tilde{S}$	transformed vector viscosity terms in ζ direction
t	time
U, V, W	velocity components in ξ, η, and ζ directions
u, v, w	velocity components in x, y, and z directions

Greek Symbols

γ	ratio of specific heats
ε	total energy per unit volume of fluid
μ	coefficient of molecular viscosity
ρ	density
ϕ	roll angle
τ	transformed time
ξ, η, ζ	transformed coordinates

<u>Subscripts</u>

B	projectile base condition
δ	total angle of attack
$wall$	wall condition
∞	free-stream condition

<u>Superscripts</u>

T	vector transpose

Note:

Aerodynamic force coefficients are defined as $\dfrac{Force}{\frac{1}{2}q_\infty(\pi d^2/4)}$

NO. OF
COPIES   ORGANIZATION

2   ADMINISTRATOR
        DEFENSE TECHNICAL INFO CTR
        ATTN DTIC DDA
        CAMERON STATION
        ALEXANDRIA VA 22304-6145

1   DIRECTOR
        US ARMY RESEARCH LAB
        ATTN AMSRL OP SD TA
        2800 POWDER MILL RD
        ADELPHI MD 20783-1145

3   DIRECTOR
        US ARMY RESEARCH LAB
        ATTN AMSRL OP SD TL
        2800 POWDER MILL RD
        ADELPHI MD 20783-1145

1   DIRECTOR
        US ARMY RESEARCH LAB
        ATTN AMSRL OP SD TP
        2800 POWDER MILL RD
        ADELPHI MD 20783-1145

        ABERDEEN PROVING GROUND

5   DIR USARL
        ATTN AMSRL OP AP L (305)

NO. OF
COPIES   ORGANIZATION

14 COMMANDER
    US ARMY ARMAMENT RD&E CTR
    ATTN AMSTA AR AET A
    M AMORUSO
    E BROWN
    S CHUNG
    A FARINA
    J GRAU
    H HUDGINS
    S KAHN
    W KOENIG
    C LIVECCHIA
    G MALEJKO
    C NG
    J THOMASOVICH
    W TOLEDO
    B WONG
    PICATINNY ARSENAL NJ 07806-5000

5   COMMANDER
    US ARMY ARMAMENT RD&E CTR
    ATTN AMSTA AR CCH B
    E FENNELL
    T LOUZEIRO
    D KITCHEN
    B KONRAD
    F QUEVEDO
    PICATINNY ARSENAL NJ 07806-5000

5   COMMANDER
    US ARMY ARMAMENT RD&E CTR
    ATTN AMSTA AR FSE
    E ANDRICOPOULIS
    K CHEUNG
    A GRAF
    D LADD
    PICATINNY ARSENAL NJ 07806-5000

6   COMMANDER
    US ARMY ARMAMENT RD&E CTR
    ATTN AMSTA AR CCL B
    D CONWAY
    D DAVIS
    K HAYES
    M PINCAY
    F PUZYCKI
    W SCHUPP
    PICATINNY ARSENAL NJ 07806-5000

1   COMMANDER
    US ARMY ARMAMENT RD&E CTR
    ATTN AMSTA AR CCH A
    J DIFUCCI
    PICATINNY ARSENAL NJ 07806-5000

NO. OF
COPIES   ORGANIZATION

1   COMMANDER
    US ARMY MISSILE COMMAND
    ATTN AMSMI RD SS AT
    B WALKER
    REDSTONE ARSENAL AL 35898-5010

3   U.S. ARMY RESEARCH OFFICE
    ATTN G ANDERSON
    K CLARK
    T DOLIGOWSKI
    PO BOX 12211
    RESEARCH TRIANGLE PARK NC 27709-2211

2   DIRECTOR
    US ARMY BENET LABORATORY
    ATTN SMCAR CCB R
    P AALTO
    S SOPOK
    WATERVALIET NY 12189

1   DIRECTOR
    US BELVOIR RD&E CTR
    ATTN SATBE FED
    N BLACKWELL
    FORT BELVOIR VA 22060-5606

2   COMMANDER
    UNITED STATES MILITARY ACADEMY
    DEPARTMENT OF CIVIL
    AND MECHANICAL ENGINEERING
    ATTN M COSTELLO
    A DULL
    WEST POINT NY 10996

6   DIRECTOR
    NASA AMES RESEARCH CTR
    ATTN MS 258-1
    L SCHIFF
    T HOLST
    D CHAUSSEE
    T EDWARDS
    G MOLVIK
    S LAWRENCE
    MOFFETT FIELD CA 94035

1   DIRECTOR
    NASA AMES RESEARCH CTR
    ATTN MS 202A-1
    M RAI
    MOFFETT FIELD CA 94035

NO. OF COPIES	ORGANIZATION	NO. OF COPIES	ORGANIZATION
3	DIRECTOR NASA LANGLEY RESEARCH CTR ATTN TECHNICAL LIBRARY J SOUTH F WILCOX LANGLEY STATION HAMPTON VA 23665	3	DIRECTOR SANDIA NATIONAL LABORATORIES ATTN MS-1511 D BARNETTE F BLOTTNER M WALKER PO BOX 5800 ALBUQUERQUE NM 87185-5800
3	COMMANDER AIR FORCE ARMAMENT LABORATORY ATTN AFATL/FXA G ABATE S ADELGREN B SIMPSON EGLIN AFB FL 32542-5434	1	DIRECTOR LOS ALAMOS NATIONAL LABORATORY ATTN MS C930 B HOGAN LOS ALAMOS NM 87545
2	COMMANDER US NAVAL SURFACE WARFARE CTR ATTN CODE R44 A WARDLAW F PRIOLO WHITE OAK LABORATORY SILVER SPRING MD 20903-5000	1	HQDA ATTN SARD TT F MILTON WASHINGTON DC 20310-0103
2	COMMANDER US NAVAL SURFACE WARFARE CTR ATTN F MOOSE T HYMES DAHLGREN VA 22448	2	HQDA ATTN SARD TR K KOMINOS S CHAIT WASHINGTON DC 20310-0103
2	COMMANDER USAF WRIGHT AERONAUTICAL LABS ATTN AFWAL/FIMG J SHANG WPAFB OH 45433-6553	3	INST FOR ADVANCED TECHNOLOGY UNIV OF TEXAS AT AUSTIN ATTN W REINECKE T KIEHNE D BARNETT 4030-2 W BRAKER LANE AUSTIN TX 78759-5329
1	COMMANDER ARNOLD ENG & DEV CTR CALSPAN FIELD SERVICE ATTN MS 600 J BENEK AAFB TN 37389	2	UNIV OF CALIFORNIA DAVIS DPT OF MECHANICAL ENGINEERING ATTN H DWYER B MEAKIN DAVIS CA 95616
2	DIRECTOR SANDIA NATIONAL LABORATORIES ATTN MS-1636 W OBERKAMPF W WOLFE ALBUQUERQUE NM 87185-5800	1	UNIVERSITY OF MARYLAND DPT OF AEROSPACE ENGINEERING ATTN J ANDERSON JR COLLEGE PARK MD 20742
		1	UNIVERSITY OF TEXAS DPT OF AEROSPACE ENGINEERING AND ENGINEERING MECHANICS ATTN D DOLLING AUSTIN TEXAS 78712-1055

ABERDEEN PROVING GROUND

5   COMMANDER
US ARMY ARMAMENT RD&E CTR
ATTN AMSTA AR FSF T
   S LIESKE
   J MATTS
   F MIRABELLE
   S PUHALLA
   J WHITESIDE

41 DIRECTOR
US ARMY RESEARCH LABORATORY
ATTN AMSRL SC CC
       R ANGELINI
       C NIETUBICZ
       J GROSH
       D HISLEY
     AMSRL SC I W STUREK
     AMSRL WT P
      A HORST
      E SCHMIDT
     AMSRL WT PA
      P CONROY
      G KELLER
      D KRUCZYNSKI
      T MINOR
      M NUSCA
     AMSRL WT PB
      H EDGE
      J GARNER
      B GUIDOS (5)
      K HEAVEY
      P PLOSTINS
      J SAHU
      P WEINACHT
     AMSRL WT PC
      G ADAMS
      R FIFER
     AMSRL WT PD
      B BURNS
      W DRYSDALE
      R LIEB
      S WILKERSON
     AMSRL WT W
      C MURPHY
     AMSRL WT WB
      F BRANDON
      T BROWN
      W D'AMICO
      D HEPNER
      M HOLLIS
     AMSRL WT WC
      J BORNSTEIN
      R VON WAHLDE

     AMSRL WT WD
      T KOTTKE
      C STUMPFEL
     AMSRL WT NC
      R LOTTERO
      S SHRAML

INTENTIONALLY LEFT BLANK.

USER EVALUATION SHEET/CHANGE OF ADDRESS

This Laboratory undertakes a continuing effort to improve the quality of the reports it publishes. Your comments/answers to the items/questions below will aid us in our efforts.

1. ARL Report Number __ARL-TR-870__ Date of Report __September 1995__

2. Date Report Received _____

3. Does this report satisfy a need? (Comment on purpose, related project, or other area of interest for which the report will be used.) _____

_____

_____

4. Specifically, how is the report being used? (Information source, design data, procedure, source of ideas, etc.)

_____

_____

_____

5. Has the information in this report led to any quantitative savings as far as man-hours or dollars saved, operating costs avoided, or efficiencies achieved, etc? If so, please elaborate. _____

_____

_____

6. General Comments. What do you think should be changed to improve future reports? (Indicate changes to organization, technical content, format, etc.) _____

_____

_____

_____

_____

CURRENT
ADDRESS

Organization

Name

Street or P.O. Box No.

City, State, Zip Code

7. If indicating a Change of Address or Address Correction, please provide the Current or Correct address above and the Old or Incorrect address below.

_____

OLD
ADDRESS

Organization

Name

Street or P.O. Box No.

City, State, Zip Code

(Remove this sheet, fold as indicated, tape closed, and mail.)
(DO NOT STAPLE)